

EXTRAPLANAR EMISSION-LINE GAS IN EDGE-ON SPIRAL GALAXIES.
I. DEEP EMISSION-LINE IMAGING

SCOTT T. MILLER^{1,2} AND SYLVAIN VEILLEUX^{2,3,4}

Department of Astronomy, University of Maryland, College Park, MD 20742;

stm, veilleux@astro.umd.edu

Draft version October 30, 2018

ABSTRACT

The extraplanar diffuse ionized gas (eDIG) in 17 nearby, edge-on disk galaxies is studied using deep Taurus Tunable Filter H α and [N II] λ 6583 images and conventional interference filter H α + [N II] λ 6548, 6583 images which reach flux levels generally below $\sim 1 \times 10^{-17}$ erg s⁻¹ cm⁻² arcsec⁻². [N II] λ 6583/H α excitation maps are available for 10 of these objects. All but one galaxy in the sample exhibit eDIG. The contribution of the eDIG to the total H α luminosity is relatively constant, of order $12 \pm 4\%$. The H α scale height of the eDIG derived from a two-exponential fit to the vertical emission profile ranges from 0.4 kpc to 17.9 kpc, with an average of 4.3 kpc. This average value is noticeably larger than the eDIG scale height measured in our Galaxy and other galaxies. This difference in scale height is probably due in part to the lower flux limits of our observations. The ionized mass of the extraplanar component inferred by assuming a constant filling factor of 0.2 and a constant pathlength through the disk of 5 kpc ranges from $1.4 \times 10^7 M_{\odot}$ to $2.4 \times 10^8 M_{\odot}$, with an average value of $1.2 \times 10^8 M_{\odot}$. Under these same assumptions, the recombination rate required to keep the eDIG ionized ranges from 0.44 to 13×10^6 s⁻¹ per cm⁻² of the disk, or about 10 to 325% of the Galactic value. A quantitative analysis of the topology of the eDIG confirms that several galaxies in the sample have a highly structured eDIG morphology. The distribution of the eDIG emission is often correlated with the locations of the H II regions in the disk, supporting the hypothesis that the predominant source of ionization of the eDIG is photoionization from OB stars located in the H II regions. A strong correlation is found between the IR (or FIR) luminosities per unit disk area (basically a measure of the star formation rate per unit disk area) and the extraplanar ionized mass, further providing support for a strong connection between the disk and eDIG components in these galaxies. The excitation maps confirm that the [N II]/H α ratios are systematically higher in the eDIG than in the disk. Although photoionization by disk OB stars is generally able to explain these elevated [N II]/H α ratios, a secondary source of ionization appears to be needed when one also takes into account other line ratios; more detail is given in a companion paper (our Paper II).

Subject headings: diffuse radiation – galaxies: halos – galaxies: ISM – galaxies: spiral – galaxies: structure

1. INTRODUCTION

The deposition of a large amount of mechanical energy at the centers of starburst and active galaxies may severely disrupt the gas phase of these systems and result in large-scale winds that may extend beyond galactic scale and influence the surrounding intergalactic medium (e.g., Chevalier & Clegg 1985; Schiano 1985; Tenorio-Tagle & Bodenheimer 1988; Tomisaka & Ikeuchi 1988; Suchkov et al. 1994; Heckman, Armus, & Miley 1990; Veilleux et al. 1994; Cecil et al. 2001, 2002). In more quiescent systems, however, the local energy inputs from individual star-forming regions are insufficient to produce large-scale winds that can blow out through the halo of the host galaxy. In this case, a “galactic fountain” may result: hot, enriched gas flows up into the halo where it cools down and eventually falls back onto the disk, presumably concentrated in clouds formed through thermal instabilities (e.g., Shapiro & Field 1976; Kahn 1981, 1991; Habe & Ikeuchi 1980; Salpeter 1985; Houck & Bregman 1990; Shapiro & Benjamin 1991). The kinematics of at least some high-velocity HI clouds in our

Galaxy may be explained in this way (e.g., Bregman 1980; Rosen & Bregman 1995). Most likely, quiescent fountaining only represents the low-energy end of a broad range of processes taking place in star-forming disks. The existence of “supershells” with 100 – 1000 pc diameters in the Milky Way and a few nearby galaxies (e.g., Heiles 1979, 1984; Brinks & Bajaja 1986; Norman & Ikeuchi 1989; Deul & den Hartog 1990; Normandeau et al. 1996) implies violent events that require the mechanical energy of a few hundred supernovae ($\sim 10^{53}$ ergs). The injection of this large amount of energy in the disk ISM may lead to the formation of vertical “chimneys” which funnel the hot gas into the halo, entraining with it the neutral and ionized ISM from the disk (e.g., Norman & Ikeuchi 1989). Galactic fountains, chimneys, and large-scale winds may all combine to create a widespread circulation of matter and energy between the disks and halos of galaxies which may be responsible for the metallicity-radius relation within galaxies and the mass-metallicity relation between galaxies (e.g., Larson & Dinerstein 1975; Vader 1986; Franx & Illingworth 1990).

Evidence for a strong interstellar disk – halo connection in

¹ Current address: Department of Astronomy, Pennsylvania State University, 525 Davey Lab., University Park, PA 16802; stm@astro.psu.edu

² Visiting Astronomer, Kitt Peak National Observatory and Cerro Tololo Inter-American Observatory, National Optical Astronomy Observatory, which is operated by the Association of Universities for Research in Astronomy, Inc. (AURA) under cooperative agreement with the National Science Foundation; Visiting Astronomer, Anglo-Australian Observatory, P.O. Box 296, Epping, NSW 1710, Australia; Visiting Astronomer, Isaac Newton Group of Telescopes, Santa Cruz de La Palma, Tenerife, Spain

³ Current address: 320-47 Downs Lab., Caltech, Pasadena, CA 91125 and Observatories of the Carnegie Institution of Washington, 813 Santa Barbara Street, Pasadena, CA 91101; veilleux@ulirg.caltech.edu

⁴ Cottrell Scholar of the Research Corporation

our Galaxy is seen at nearly all wavelengths. Pulsar dispersion measures (e.g., Guélin 1974; Taylor & Manchester 1977), free-free absorption of low-frequency galactic radio emission (Ellis 1982), ultraviolet absorption lines (e.g., York 1983) and faint, optical emission lines (Reynolds, Scherb, & Roesler 1973; Reynolds, Roesler, & Scherb 1974; Reynolds 1980) point to the existence of a widespread, ionized component of interstellar gas extending to large heights above the plane of the Galaxy. Often called the Reynolds layer, this component consists of a low-density ($0.2 - 0.4 \text{ cm}^{-3}$), $2 - 3 \text{ kpc}$ thick layer of warm ($\sim 10^4 \text{ K}$), ionized material that has an emission-line spectrum which differs from that of typical H II regions (e.g., Reynolds, Roesler, & Scherb 1977; Reynolds 1985a, 1985b, 1988, 1990; Kulkarni & Heiles 1988; Reynolds & Tufté 1995; Haffner, Reynolds, & Tufté 1999). The Reynolds layer appears to act as an interface between the dense star-forming ISM in the Galaxy midplane and the hot, diffuse Galactic corona (e.g., Rosen & Bregman 1995; de Avillez & Berry 2001).

Support for dynamically active disks in external galaxies comes from a wide variety of observations, including the detection of supershells in the disks of nearby gas-rich systems (e.g., LMC; Kim et al. 1999), thick radio disks in edge-on spirals (e.g., Ekers & Sancisi 1977; Allen et al. 1978; Hummel & van der Hulst 1989; Hummel & Dettmar 1990; Hummel, Beck, & Dahlem 1991a; Hummel, Beck, & Dettmar 1991b; Hummel et al. 1991c; Dahlem, Dettmar, & Hummel 1994; Golla & Hummel 1994; Dahlem, Lisenfeld, & Golla 1995; Irwin, English, & Sorathia 1999; Tüllman et al. 2001), and extraplanar dust and line-emitting filaments in edge-on disk systems (e.g., Dettmar 1992; Dahlem 1997 and references therein). The most prominent example of extraplanar diffuse ionized gas (eDIG) outside of our Galaxy is seen in the nearby edge-on Sb galaxy NGC 891, considered by many to be a near twin of our own Galaxy. Optical line-emitting filaments that extend out to distances of $\sim 4.5 \text{ kpc}$ above the disk of the galaxy are seen superposed on diffuse emission extending over an area of $\sim 5 \text{ kpc}$ in diameter and with scale height of $2 - 3 \text{ kpc}$ (e.g., Dettmar 1990; Rand, Kulkarni, & Hester 1990; Sokolowski & Bland-Hawthorn 1991; Dettmar & Schultz 1992; Pildis, Bregman, & Schombert 1994a; Rand 1997, 1998; Hoopes, Walterbos, & Rand 1999; Howk & Savage 2000; Collins & Rand 2001). The eDIG in NGC 891 shares a resemblance with the Reynolds layer in our own Galaxy and, for this reason, NGC 891 is usually the Rosetta stone to which all other galaxies are compared when discussing eDIG.

Results from emission-line imaging surveys suggest that few edge-on spirals show evidence of a widespread diffuse ionized medium like that of our Galaxy and NGC 891, but these observations often reveal kpc-scale filaments and plumes which may represent the bright features of a more extensive but fainter complex of high- $|z|$ material (see, e.g., Dettmar 1992; Pildis, Bregman, & Schombert 1994b; Veilleux, Cecil, & Bland-Hawthorn 1995; Rand 1996; Hoopes et al. 1999). Few constraints exist on the full extent of the eDIG in these galaxies. This question is directly relevant to $\text{Ly}\alpha$ absorption systems seen in quasar spectra since the eDIG may contribute significantly to the gaseous cross-section of star-forming disk galaxies. Giant ($\sim 15 \text{ kpc}$) $\text{H}\alpha$ -emitting halos have been purported to exist in the edge-on galaxies NGC 4631 and NGC 4656 (Donahue et al. 1995), but unpublished Fabry-Perot observations do not seem to confirm this finding (S. N. Vogel 2003, private communication). Dahlem et al. (1996) have detected a

soft X-ray halo in NGC 3628 which extends to 25 kpc , but this galaxy is apparently undergoing a starburst-driven wind event which is considerably more energetic than the phenomena taking place in quiescent star-forming disks (see also Bregman & Pildis 1994; Wang et al. 1995; Bregman & Houck 1997; Dahlem, Weaver, & Heckman 1998).

In an attempt to refine our knowledge on the eDIG of nearby galaxies, we have carried out an emission-line imaging survey of a moderately large sample of edge-on disk galaxies down to flux levels of several $\times 10^{-18} \text{ erg s}^{-1} \text{ cm}^{-2} \text{ arcsecond}^{-2}$, often about an order of magnitude fainter than that of most published surveys. The criteria used in selecting the sample of galaxies are described in §2. The methods used to acquire and reduce the images are discussed in §3 and §4. The empirical results from the image analysis are given in §5 while a quantitative analysis of the eDIG morphology is carried out in §6. In §7, the morphological properties of the eDIG are compared with the properties of the host galaxies to shed new light on the origin of the eDIG in these objects. A summary of the results is given in §8. A companion paper (Miller & Veilleux 2003; hereafter Paper II) describes the results from long-slit spectroscopy of the eDIG.

2. SAMPLE

The galaxies in the sample are listed in Table 1. These 17 objects were selected based on inclination, proximity, angular size, and lack of companions. The sample was limited to edge-on galaxies with an inclination larger than $\sim 80^\circ$ with the majority of them having $i > 85^\circ$. This was done to facilitate separation of the disk emission from that of the halo. Even with this sample, inclination biases may affect some of the eDIG parameters. At 85° , a galaxy with a radius of 10 kpc will have a projected radius of $\sim 0.9 \text{ kpc}$ in the plane of the sky, and at 80° , the radius will be projected $\sim 1.7 \text{ kpc}$ in the plane of the sky. Inclination effects are discussed in more detail in §5 and §7, when relevant.

Nearby ($z < 0.1$) galaxies were selected to provide good spatial resolution. Most of the sample galaxies have a spatial resolution better than 300 pc , enough to resolve an average H II region (see, e.g., Hodge 1987, although recent HST observations suggest that H II regions can be, on average, as small as 50 pc ; e.g., Scoville et al. 2001). One should note, however, that the galaxies in our sample cover a relatively broad range in distance ($1.6 - 63 \text{ Mpc}$). The impact of possible distance-related biases on the results of our study is discussed in §5 and §7. NGC 55 and NGC 973 are by far the nearest and furthest galaxy in our sample and are sometimes excluded from the analysis to reduce the range in distance covered by the sample.

The sample galaxies were also chosen so that they would easily fit within the field of view of the imager ($D_{25} < 7'$ for all galaxies, with the exception of NGC 55) and allow us to use the shift and stare method to build “super” sky flats (see §4.1). Finally, the sample was generally limited to galaxies with no known companion(s) within $5'$ in order to avoid contamination from tidal features such as warps, bridges, or tails which may extend far from the galactic plane (NGC 2820 and NGC 3432 are the only two clear exceptions in the sample; IC 1815 is located $4.6'$ from NGC 973, but there are no obvious signs of interaction between these two objects).

3. DATA ACQUISITION

3.1. Conventional Narrow-band Imaging

Ten of the sample galaxies were observed with traditional techniques at either the Kitt Peak National Observatory (KPNO) or the Cerro Tololo Inter-American Observatory (CTIO) facilities during three observing runs. Complete details of the observations can be found in Table 2, including the telescopes and filters used for these observations as well as the total exposure times, number of exposures, field of view, and spatial scale (after binning, when relevant; see §4). Narrow-band filters were chosen such that the redshifted $H\alpha$ emission of each galaxy fell near the center of the filter bandpass.

An important goal of this survey is to image the galaxies down to a surface brightness at $H\alpha$ of $\sim 1 \times 10^{-17}$ erg s^{-1} cm^{-2} arcsec $^{-2}$ or below. In order to reach this faint flux level, great care was taken in both the acquisition and reduction of the data. One of the greatest problems in accurate data reduction is the inconsistency in the sky background of each image. Since the total exposure time for each galaxy is on the order of hours, it is difficult to maintain a constant sky background over this length of time. Both the change in the zenith angle of the object (and thus the airmass) as well as the sky photometry can lead to inconsistencies in the background which need to be carefully corrected.

To reduce long-term photometric variations, short-exposure $H\alpha$ and Gunn r -band continuum observations were obtained alternatively. The exposures were long enough, though, to insure that each frame was dominated by sky noise. The CCD used for the KPNO 0.9-m observations (but not for the CTIO Curtis Schmidt observations) was spatially binned 2×2 to increase the signal rate per pixel from the diffuse emission. The Poissonian sky background noise dominates over the read-out noise, and so binning the data 2×2 does not affect the signal-to-noise ratio of the data for a given exposure time but allowed us to take shorter exposures, thus enabling us to take more images in one night. This is important for the shift and stare method (see §4.1) and helps average out temporal variations and reduce the number of cosmic rays per frame. The resulting spatial resolution of the KPNO data is still better than that of the CTIO Curtis Schmidt observations (Table 2).

3.2. Taurus Tunable Filter Imaging

Ten galaxies were also observed with the The Taurus Tunable Filter (TTF) at the Anglo-Australian Telescope (TTF) and William Herschel Telescope (WHT). This instrument is able to achieve the same desired flux levels (i.e. $\lesssim 1 \times 10^{-17}$ erg s^{-1} cm^{-2} arcsec $^{-2}$) in much less time. Developed at the Anglo-Australian Observatory, the TTF design is based on the concept of a conventional Fabry-Perot (FP) interferometer. Using two parallel plates of high reflectivity, light travels through the interferometer such that at each radius from the optical axis a specific wavelength is imaged, resulting in the wavelength varying quadratically with distance from the optical axis. The TTF is able to maintain plate parallelism down to $\sim 2 \mu\text{m}$ and scan over a range of $\sim 10 \mu\text{m}$. This allows the instrument to work at low orders of interference and thus ensures that the wavelength varies little ($\lesssim 18 \text{ \AA}$) over the full field of view. In other words, it is now possible to obtain quasi-monochromatic images with a single exposure. In addition, the TTF has the ability of adjusting the bandwidth of the filter from ~ 6 to 60 \AA , thus making it possible to obtain very narrow-band images. This allowed us to separate the $H\alpha$ and [N II] $\lambda 6583$ emission lines, a difficult task with conventional narrow-band filters.

The TTF at the AAT also has the ability to switch between

frequencies at a very rapid rate, up to ~ 100 Hz if needed. By shuffling the charge of the CCD in sync with the frequency switching, it is possible to observe an object at two distinct frequencies (and two distinct bandwidths) *at almost the same time*. This technique allowed us to average out any sky variations over both frames. For our observations, redshifted $H\alpha$ and [N II] $\lambda 6583$ were observed alternatively every 2 minutes for several cycles, thus yielding very low flux levels and more precise, two-dimensional [N II]/ $H\alpha$ maps. Unfortunately, the WHT did not have charge shuffling and frequency switching capabilities at the time of the observations, but the use of the TTF in obtaining very narrow-band quasi-monochromatic images still allowed us to reach the faint flux levels desired in less time than it would have taken using conventional methods. A more complete description of the TTF capabilities can be found in Bland-Hawthorn & Jones (1998; see also the TTF web page <http://www.aao.gov.au/ttf>).

Three of the galaxies observed with the TTF are in common with the KPNO/CTIO sample (NGC 55, NGC 2424, and NGC 3044). This overlap allows us to assess the impact of lower spatial resolution on the KPNO and CTIO data. Full details about the TTF runs are listed in Table 3. The etalon was tuned to a bandpass of $\sim 13 - 16 \text{ \AA}$, allowing us to obtain separate $H\alpha$ and [N II] images for these galaxies. An intermediate blocking filter [$\Delta\lambda(\text{AAT}) = 210 \text{ \AA}$; $\Delta\lambda(\text{WHT}) = 280 \text{ \AA}$] was used to block out all but one order of interference through the TTF. The charge shuffling and frequency shifting capabilities at the AAT was used to obtain simultaneous images of $H\alpha$ and [N II], while continuum images were taken separately. At the WHT, each image was taken individually. Because the galaxies filled a significant fraction of the frame, we could not use the shift and stare method, but the capabilities of the TTF in reaching faint flux levels more than compensated for the relatively modest field of view of $\gtrsim 8'$. The position of the galaxies in each frame was shifted slightly between observations to allow us to reject bad pixels when the frames were combined together.

A neon calibration cube was obtained before and after each galaxy observation to determine the wavelength calibration in relation to spatial position and etalon gap spacing. The free spectral range (i.e. the wavelength range between orders) was 230 \AA for the AAT and 280 \AA for the WHT; both were larger than, or equal to, the blocking filter width and thus ensured that only one order was imaged.

4. DATA REDUCTION

4.1. KPNO and CTIO data

The data sets were reduced using standard IRAF packages. A mean bias frame was calculated and subtracted from each image making sure that no additional noise was added to the images. ‘‘Super’’ sky flats were created using the shift and stare method. As opposed to dome flats and normal sky flats, which are not taken at the same time as the objects (and thus cannot truly correct for the conditions present during the actual observation), ‘‘super’’ sky flats were constructed using the object images themselves. For each $H\alpha$ – continuum exposure pair, the frame was shifted such that the position of the galaxy was in a different section of the image in each exposure. Using this method, about 20 to 30 exposures were acquired for each galaxy.

Bright objects were masked out using the IRAF FOCAS add-on package, resulting in a more accurate representation of the flatfield response *at the time of the observations*. The images

were then combined together, rejecting anomalously high and low pixels that were not masked out by the FOCAS routines. Because each observation of the galaxy was positioned in different regions of the frame, each pixel in the combined frame is well sampled (i.e., not masked out due to a bright object). When possible, separate sky flats were created for each object and each night so that variations in the observations were minimized. These accurate sky flats enabled us to achieve lower flux levels than possible with conventional flats. Note, however, that contamination by Galactic [N II] $\lambda 6583$ emission from the Reynolds layer (which is known to vary on sub-arcminute angular scale) and scattering in the telescope and filter limit the accuracy of this technique.

The images were flatfielded using the sky flats and then aligned. Finally, the images were corrected for airmass and the sky background was subtracted. The sky background was determined interactively using regions uncontaminated by the galaxies or other bright objects in order to ensure that it was not affected by low surface brightness emission. The images were then flux calibrated using observations of standard flux calibrators (Stone 1977, Stone & Baldwin 1983, Landolt 1992a, 1992b). The IRAF COMBINE package was used to not only add the individual frames together but also remove cosmic rays.

In order to remove the presence of continuum emission in the narrow-band images, the galaxies were also observed with an intermediate-band ($\sim 800 - 900 \text{ \AA}$ FWHM) Gunn r filter. These images were obtained and reduced following the same procedures used for the narrow-band images, and then subtracted from the narrow-band images in order to obtain the $H\alpha + [\text{N II}]\lambda 6583$ images. The delicate procedure of continuum subtraction is described in more detail in §4.3 below.

This method of data reduction has allowed us to observe down to an average flux level of $\sim 1 \times 10^{-17} \text{ erg s}^{-1} \text{ cm}^{-2} \text{ arcsec}^{-2}$ (the 2σ flux limit for each galaxy is listed in Table 2).

4.2. Taurus Tunable Filter Data

The TTF data were reduced using the Zodiac data reduction package (which was first developed at the University of Hawaii/IfA by George Miyashiro) as well as standard IRAF packages, following the procedures described in Jones, Shopbell, & Bland-Hawthorn (2002). The bias structure was relatively constant over the images, therefore a constant bias was subtracted from each. The data were flatfielded using traditional sky flats/dome flats as required. Bright objects were masked out and a mean sky value was calculated in annular bins around the optical axis. An azimuthally symmetric sky frame was produced from this sky radial profile for each image and subtracted off. In all cases, the field of view of the TTF was large enough to derive accurate sky levels using regions free of galaxy emission. The data were flux calibrated using observations of standard flux calibrators (Stone & Baldwin 1983; Massey et al. 1988). Cosmic rays were detected and removed, and the images for each galaxy were then aligned and summed together.

In order to remove continuum emission from each galaxy, Cousins R -band continuum images were obtained as well. These images were reduced in a similar fashion to the TTF images and subtracted from them in order to obtain individual $H\alpha$ and [N II] $\lambda 6583$ images for each galaxy. The continuum subtraction method is described next.

4.3. Continuum Subtraction

Obtaining continuum subtracted emission-line images is not straightforward. The obvious approach is to scale the continuum image such that the foreground stars are perfectly subtracted; unfortunately, there are problems with this simple approach. First, the stellar population of the galaxies differs from that of the field stars, and so the scaling factor for the field stars is different from that of the galaxies. Second, and more importantly, the stellar population in the bulge of the galaxy differs from that in the disk of the galaxy, so ideally the continuum needs to be scaled differently in these two regions. In this study, we decided to use an iterative process in which the scaling factor of the continuum image is determined from the overall morphology of the residual emission-line image. Radial cuts of the continuum-subtracted image are examined to determine if oversubtraction has occurred. Oversubtraction of the continuum image is noticeable as a dip in the vertical profile below the background of the emission-line map.

5. EMPIRICAL RESULTS

The continuum-subtracted emission line images of each galaxy in the sample are presented in Figure 1 – 17 and discussed in the Appendix. [N II] $\lambda 6583/H\alpha$ excitation maps are also presented for 10 of the galaxies in the sample. The present section discusses the overall trends found in the sample. For a more detailed discussion of each object, the reader should refer to the Appendix.

5.1. Integrated $H\alpha$ Luminosities

The integrated $H\alpha$ luminosity for each galaxy (measured within the field of view) is listed in Table 4. In an effort to compare values between galaxies of different sizes, we also derive the $H\alpha$ luminosity/ D_{25}^2 , or the total $H\alpha$ luminosity divided by the square of the apparent isophotal diameter (at a surface brightness level $\mu_B = 25.0 \text{ B mag arcsec}^{-2}$). This quantity gives only a basic indication of the $H\alpha$ luminosity per unit disk area for each galaxy, since only a fraction of the total $H\alpha$ luminosity is detected in these highly inclined galaxies. Due to uncertainties in the continuum subtraction and flux calibration, typical uncertainties for the $H\alpha$ luminosity are $\sim 10 - 25\%$. The KPNO and CTIO data were corrected for contamination by the nearby [N II] lines. While studies indicate that the [N II]/ $H\alpha$ ratio increases with increasing $|z|$ (e.g., see §5.6 and Paper II and references therein), a constant ratio of [N II] $\lambda 6583/H\alpha = 0.5$ and [N II] $\lambda 6548/H\alpha = 0.17$ was assumed for the entire DIG in order to simplify the calculations.

The $H\alpha$ luminosities in the galaxies of our sample range from $3.4 \times 10^{39} \text{ erg s}^{-1}$ to $83 \times 10^{39} \text{ erg s}^{-1}$, with an average value of $32 \times 10^{39} \text{ erg s}^{-1}$, and $L(H\alpha)/D_{25}^2$ ranges from $0.8 \times 10^{37} \text{ erg s}^{-1} \text{ kpc}^{-2}$ to $40 \times 10^{37} \text{ erg s}^{-1} \text{ kpc}^{-2}$, with an average value of $6.2 \times 10^{37} \text{ erg s}^{-1} \text{ kpc}^{-2}$ (see Table 4 and Fig. 18). These results can be compared with published measurements in three cases: NGC 55 (Hoopes, Walterbos, & Greenwalt 1996; Ferguson, Wyse, & Gallagher 1996; Otte & Dettmar 1999), NGC 2188 (Domgörgen & Dettmar 1997), and NGC 3044 (Rossa & Dettmar 2000). For NGC 55, our value of $8.9 \times 10^{39} \text{ erg s}^{-1}$ is only about half of what Hoopes et al. and Ferguson et al. measure for the $H\alpha + [\text{N II}]$ luminosity (2.6 and $2.0 \times 10^{40} \text{ erg s}^{-1}$, respectively), but taking the [N II] contamination into account brings their values closer to our measurements. Rather than list the luminosity, Otte & Dettmar list an $H\alpha$ flux of $2.8 \times 10^{-11} \text{ erg s}^{-1} \text{ cm}^{-2}$. Converting their flux to a luminosity (using a distance to NGC 55 of 1.6 Mpc), one ob-

tains a luminosity of 8.58×10^{39} erg s⁻¹, very similar to ours. For NGC 2188, the difference in H α luminosity between our value of 9.91×10^{39} erg s⁻¹ and Domgörgen & Dettmar’s value of 1.1×10^{40} erg s⁻¹ lies within the uncertainties of the measurements. Finally, our H α luminosity for NGC 3044 of 8.94×10^{40} erg s⁻¹ differs slightly but not significantly from Rossa & Dettmar’s value of 1.27×10^{41} erg s⁻¹.

5.2. Detection Frequency, H α Luminosity, and Scale Height of the eDIG

In order to study the eDIG, one first needs to define this term. This is non-trivial since the boundary between the disk H II regions and the eDIG is not clearly defined; the line emission smoothly changes from one component to the other with no obvious break in the emission profile. The typical size of an H II region which is resolvable from the ground is on the order of 300 pc (Hodge 1987), so a vertical cutoff at this height might be appropriate. However, since the sizes of H II regions undoubtedly vary with location within the galaxy as well as with galaxy type, this definition is not adequate.

The scale height of the continuum emission is a better guideline. This scale height was derived at each radius in the galaxy using an exponential fit to the continuum image, excluding the inner 300 pc so that dust obscuration would not affect the results. This scale height was then used as a first iteration for the lower boundary of the extraplanar gas. A mask was created such that all continuum emission within a vertical scale height of the midplane of the disk was excluded, and this mask was multiplied by the H α image so that only the extraplanar gas outside of one vertical (continuum) scale height remained. For comparison, an H II region mask was also created using the H α equivalent width criterion described in Bland-Hawthorn, Sokolowski, & Cecil (1991). It was found that the scale-height mask did not completely exclude all of the H II regions defined by the equivalent-width mask. The extent of the scale-height mask was varied until it did exclude the H II regions; it was found that a mask based on a vertical extent of about $1.25 \times$ the continuum scale height worked well in that it excluded the H II regions but did not extend much further past them vertically. This method was adopted to define the eDIG component in all of the galaxies of the sample. The resulting vertical height of the masked region is roughly constant with radius within each galaxy, but varies among the different galaxies from ~ 500 pc to 3 kpc. This broad range in continuum scale heights is mainly due to variations in the inclinations of the galaxies.

Extraplanar DIG is detected in nearly all of the galaxies in the sample. Only one galaxy, ESO 209-9, does not provide enough evidence to warrant further investigation; the lack of obvious eDIG in this object may be due to an unfortunate combination of observational factors (e.g., relatively high flux limits and poor spatial resolution). Although most of the galaxies in the sample do not show widespread diffuse ionized emission as pervasive as in NGC 891 (one possible exception is NGC 2188, where extraplanar emission is detected over a radius of 4 kpc; this emission may even extend further since the detection was limited by the field of view of the AAT setup; see also Domgörgen & Dettmar 1997), many of them show localized regions of eDIG emission often characterized by distinct filaments or plumes extending up a few kpc from the plane of host galaxy. The topology of the eDIG is analysed more quantitatively in §6.

The eDIG emission has an average luminosity of 4.4×10^{39} erg s⁻¹ and ranges from 0.12×10^{39} erg s⁻¹ to 13×10^{39}

erg s⁻¹, and comprises $12 \pm 4\%$ of the total luminosity of the galaxies (Table 4 and Fig. 18; the eDIG fraction is $13 \pm 5\%$ if we exclude NGC 55 and the 6 galaxies in the sample with $i < 85^\circ$). All but four galaxies (NGC 55, ESO 362-11, NGC 3432, NGC 4013), have values that lie within 10 – 16%, suggesting that the luminosity of the ionized H α halo is a fairly constant fraction of the total H α luminosity of the galaxy. All four galaxies with low eDIG/total luminosity ratios clearly show the presence of extraplanar ionized gas, so it is not clear why the ratios for these galaxies are lower than average.

Exponential curves were fit to the vertical profile of each H α image to determine the scale height of the line-emitting gas. In most galaxies, the inner 300 pc are excluded in order to mask out contamination by H II regions or dust lanes (a few galaxies require excluding more than the inner 300 pc; e.g., NGC 3628). Both one- and two-exponential fits were used to model the diffuse emission. The fits are shown in Figure 19. Wang et al. (1997) discuss Rand’s (1997) use of a two-exponential fit and suggest that the two components represent a quiescent component and a disturbed component of the DIG, which they identify kinematically. They use this distinction between the two to define the fainter, more disturbed component as the “extraplanar” component of the DIG; we adopt the same definition from here on out. The eDIG scale heights for the galaxies in the present sample are listed in Table 5 and range from 0.4 kpc to 17.9 kpc, with an average of 4.3 kpc (Fig. 18; the average eDIG scale height is 5.0 kpc if we exclude NGC 55 and the 6 galaxies in the sample with $i < 85^\circ$). This average value is noticeably larger than the eDIG scale height in our Galaxy (0.75 kpc; Reynolds 1989, 1990) or in NGC 891 (0.5 kpc; Dettmar 1990). In a study of nearby edge-on galaxies, Hoopes et al. (1999) find scale heights ranging from 450 pc to 1.7 kpc, again smaller on average than the values found in our galaxies. This difference in scale height is due to our definition of the eDIG and to the fainter flux levels reached by our observations. The better sensitivity of our observations allows us to study a previously undetected eDIG component above galaxy disks.

The emission measure, $EM = \int n_e^2 dl$, is related to the H α intensity by

$$EM = 2.75 \times T_4^{0.9} I_{H\alpha} \text{ cm}^{-6} \text{ pc} \quad (1)$$

with $I_{H\alpha}$ given in Rayleighs ($1 \text{ R} = 5.66 \times 10^{-18} \text{ erg s}^{-1} \text{ cm}^{-2} \text{ arcsec}^{-2}$ at H α), T_4 is the gas temperature in units of 10^4 K , and dl is given in units of parsecs (e.g., Reynolds 1990). The emission measure in the midplane of the galaxy is derived using the H α intensity at $|z| = 0$, extrapolated from the two-exponential fit to the vertical profiles (see Table 5). This quantity is an emission measure determined in the midplane of the disk from the observed, edge-on orientation and is an average over all radii since it is derived from the average vertical profile of each galaxy.

The average value for the emission measure in the midplane associated with the extraplanar gas (based on the second component of the two-exponential fits) is 14 pc cm^{-6} , but ranges in value from 0.39 pc cm^{-6} to 69 pc cm^{-6} (Fig. 18). For comparison, Hoopes et al. (1999) find midplane emission measures of $\sim 2 - 10 \text{ pc cm}^{-6}$ (except for NGC 891, which has a midplane emission measure of $\sim 25 - 45 \text{ pc cm}^{-6}$). A careful examination of our data shows that the galaxies with the largest scale heights have some of the lowest midplane emission measures (e.g., ESO 240-11 and NGC 5965), suggesting again that the present low-flux-level observations are detecting a very faint, extraplanar region of diffuse ionized gas. Galaxies with

large midplane emission measures (e.g., NGC 2188, NGC 55, & NGC 1507) have small scale heights ($\sim 400 - 800$ pc). Only one galaxy, NGC 3044, has sizeable midplane emission measures [16 (North) and 62 (South) pc cm $^{-6}$] and scale heights [2.8 (North) and 1.3 (South) kpc]. The midplane emission measures and scale heights of the galaxies in our sample have a Pearson's probability $P[\text{null}] \approx 0.024$ for the null hypothesis of zero correlation, indicating a weak anti-correlation between these two quantities. This anti-correlation is consistent with the predictions of hydrodynamical simulations of star-forming disk galaxies. For instance, Rosen & Bregman (1995) find that as the energy flow rate from the disk to the halo is increased, the midplane electron density ($\propto \text{EM}^{0.5}$) decreases while the gas scale height increases.

5.3. Midplane Density & Mass of the eDIG

Given the emission measure at the midplane of a galaxy, the electron density at this location can be estimated using $\text{EM} = n_e^2 f l$, where l is the length of the line of sight through the volume of gas and f is the filling factor (assumed to be constant with height). For simplicity, we assume $f = 0.2$ at all z , as determined in the midplane of our Galaxy (Reynolds 1990), and use a line-of-sight length $l = 5$ kpc (Veilleux et al. 1995). This gives an electron density of

$$n_e(z) = 3.16 \times 10^{-2} \text{EM}(z)^{0.5} \left(\frac{0.2}{f}\right)^{0.5} \left(\frac{5 \text{ kpc}}{l}\right)^{0.5} \text{cm}^{-3}. \quad (2)$$

The calculated electron density can then be used to determine the mass of the ionized gas. Using $M = \int \rho dV$ and assuming $n_e \sim n_p$, we get

$$M \approx \int n_e(z) m_p dV, \quad (3)$$

where m_p is the mass of a proton. Since $n_e \propto \text{EM}^{0.5}$, the scale height of the electron density is twice that of the emission measure. If we assume that this scale height represents the extraplanar extent of the gas and calculate the eDIG mass for each side of a galaxy, equation (3) then becomes

$$M \approx 2 \pi n_e(z=0) m_p H_z R^2, \quad (4)$$

where H_z is the scale height of the extraplanar gas emission and R is the optical radius of the galaxy. The electron density at $z = 0$ and ionized mass are listed in Table 5 and their distributions are shown in Figure 18. Values in the Table are calculated for both the one-exponential fit and both components of the two-exponential fits, but Figure 18 only shows the distribution of the one-sided eDIG masses derived from the second component of the two-exponential fits.

The midplane electron densities of the eDIG derived from the two-exponential fits range from 0.020 cm^{-3} to 0.26 cm^{-3} , with an average value of 0.11 cm^{-3} , and the total (two-sided) extraplanar ionized masses range from $1.4 \times 10^7 M_\odot$ to $2.4 \times 10^8 M_\odot$, with an average value of $1.2 \times 10^8 M_\odot$ (the average value for the total eDIG mass becomes $1.5 \times 10^8 M_\odot$ if we exclude NGC 55 and the 6 galaxies in the sample with $i < 85^\circ$). For comparison, Rand (1996) derives values for $n_e(z=0)$ in the range of $0.16 - 0.3 \text{ cm}^{-3}$, on average slightly larger than the values derived in our study. Rossa & Dettmar (2000) measure eDIG masses ranging from 1.8 to $13 \times 10^6 M_\odot$. These values are considerably smaller than the values derived here. This discrepancy with our data arises primarily from the fact that Rossa & Dettmar use a different method to calculate the mass of diffuse ionized gas. Another source of discrepancy is the better sensitivity of our observations which allows us to detect fainter eDIG emission.

5.4. Recombination Rate Requirements

The $\text{H}\alpha$ intensity, scale height, and electron density of the eDIG can be used to estimate the recombination rate in a column perpendicular to the galactic plane using

$$\eta_{\text{DIG}} = \int \alpha(T) n_e^2(z) dz = \alpha(T) f \langle n_e^2(z=0) \rangle H_z, \quad (5)$$

where the value of the Case B recombination coefficient, $\alpha_B(T)$ is equal to $2.58 \times 10^{-13} \text{ cm}^3 \text{ s}^{-1}$ at $T = 10^4 \text{ K}$ (Martin 1988), f is the filling factor, which we again assume to be constant at 0.2, n_e is the electron density of the eDIG at $z = 0$, and H_z is the scale height of the eDIG emission. Substituting the eDIG electron densities and scale heights listed in Table 5, we find that η_{DIG} varies from 0.44 to $13 \times 10^6 \text{ s}^{-1} \text{ per cm}^{-2}$ of the disk, with an average of $3.6 \times 10^6 \text{ s}^{-1} \text{ per cm}^{-2}$ (the average value for the recombination rate becomes $4.6 \times 10^6 \text{ s}^{-1}$ if we exclude NGC 55 and the 6 galaxies in the sample with $i < 85^\circ$). For comparison, the diffuse interstellar medium in our Galaxy requires a recombination rate of $4 \times 10^6 \text{ s}^{-1} \text{ per cm}^{-2}$ of galactic disk (Reynolds 1984).

5.5. [N II] $\lambda 6583/\text{H}\alpha$ Excitation Maps

[N II] $\lambda 6583/\text{H}\alpha$ ratio maps have been derived for all ten objects in the sample for which TTF data are available. They are presented in the Appendix. Artifacts of the data acquisition and reduction are affecting these maps. In a few cases, a slight mismatch in the central wavelengths of the $\text{H}\alpha$ and [N II] images is apparent, causing artificial [N II]/ $\text{H}\alpha$ gradients along the galaxy disks where the velocity gradients are steepest (NGC 2188, NGC 3044, ESO 362-11). Reflective ghosts are also a problem in two objects, causing the arc-like gradient in the excitation map of NGC 55 and substructures in the map of NGC 891. One therefore has to be careful when interpreting these maps. Nevertheless, general statements about the excitation properties of the eDIG can be made from these data.

It is clear that the [N II]/ $\text{H}\alpha$ ratios in the eDIG are generally larger than in the disk. Arguably the cleanest case for this effect is NGC 4013, where the [N II]/ $\text{H}\alpha$ ratios are H II region-like in the disk but reach values close to unity in the eDIG. A vertical [N II]/ $\text{H}\alpha$ gradient is also easily detected in NGC 891, and is visible but more shallow in NGC 1507, NGC 2188, NGC 3044 and possibly ESO 362-11. These results confirm the conclusions of previous studies in these and other galaxies (e.g., Keppel et al. 1991; Dettmar & Schultz 1992; Veilleux et al. 1995; Golla, Dettmar, & Domgörgen 1996; Domgörgen & Dettmar 1997; Rand 1998, 2000; Tüllman & Dettmar 2000; see also the Appendix and Paper II). We also confirm the systemic trend of increasing [N II]/ $\text{H}\alpha$ ratio with decreasing $\text{H}\alpha$ surface brightness found in NGC 55 by Ferguson, Wyse, & Gallagher (1996) and Otte & Dettmar (1999). A similar effect is seen in NGC 7817.

Photoionization models (e.g., Mathis 1986; Domgörgen & Mathis 1994; Sokolowski 1994; Bland-Hawthorn et al. 1997; Mathis 2000) have had some success explaining the increase in the [N II]/ $\text{H}\alpha$ line ratio observed in the eDIG. This increase is attributed to a decrease with height of the ionization parameter (U), a measure of the ratio of the ionizing photon number density (Φ) to the electron density (n_e). Under the assumption of ionization equilibrium, $\Phi \propto n_e^2$ at all heights. Therefore, U

$\propto \Phi/n_e \propto n_e$, so the ionization parameter should fall off exponentially with height. As U decreases, lower ionization species are favored, leading to an increase in the $[\text{N II}]/\text{H}\alpha$ ratio. More quantitatively, however, photoionization models have difficulties reproducing $[\text{N II}] \lambda 6583/\text{H}\alpha$ in excess of unity unless one takes into account the multi-phase nature of the ISM, the possible depletion of certain gas-phase abundance of metals onto dust grains, and the absorption and hardening of the stellar radiation field as it propagates through the dusty disk (Sokolowski 1994; Bland-Hawthorn et al. 1997). The line ratios measured from the present data are generally less than ~ 1.5 and can therefore be explained from OB photoionization. More line ratios are needed to better constrain the source of ionization of the eDIG. This issue is re-examined in Paper II, where we present the results from deep long-slit spectroscopy of several edge-on spirals. In that paper, we find that photoionization by massive OB stars alone generally has difficulties explaining all of the line ratios in the extraplanar gas. Hybrid models that combine photoionization by OB stars and another source of ionization such as photoionization by turbulent mixing layers or shocks provide a better fit to the line ratios in the eDIG.

6. MORPHOLOGICAL ANALYSIS OF THE EDIG

6.1. *Spatial Correlation between Disk and Extraplanar Emission*

The extraplanar emission is summed vertically to derive the brightness profile of the eDIG as a function of galactocentric radius. The same is done with the emission coming from the H II regions in the disk. Next, a cross-correlation analysis is carried out between the radial profiles of the disk emission and eDIG emission in the hopes of quantifying possible spatial correlations between these two components. Note, however, that dust in the disk of the galaxies is almost certainly obscuring some of the disk $\text{H}\alpha$ emission and thus skewing the results. The results of this correlation analysis should therefore be used with caution and in combination with other morphological indicators.

Figure 20 displays the radial disk and eDIG emission profiles for each galaxy. Also shown in this figure are the results of the cross-correlation analysis for each side of the extraplanar emission. The correlation coefficient is plotted as a function of the radial shift between the disk and eDIG profiles. A correlation coefficient of 1 (−1) signifies a perfect (anti-)correlation. All galaxies demonstrate some degree of correlation between the disk and halo emission. The correlation coefficients generally peak at or near zero radial shift, but the peak value varies from one galaxy to the next. The values of the coefficients at zero radial shift are used in the following discussion to assess the degree of correlation. These values are listed in Table 6.

The profile of the correlation coefficient also provides a rough measure of the topology of the extraplanar gas. Galaxies with extraplanar filaments ionized by nearby disk H II regions are expected to produce more strongly peaked correlation profiles than galaxies in which the extraplanar gas is ionized by a more diffuse source. Galaxies with widespread extraplanar emission may show significant correlation with the disk, but their correlation profiles should be broad since the diffuse emission is not necessarily tied to specific locations in the disk.

The average amplitude of the correlation peaks at zero radial shift is found to be 0.60 ± 0.24 . The majority of the galaxies in the sample therefore show significant correlation between the disk and halo components. Roughly 50% of the galaxies in the sample show sharply peaked correlation profiles with $\text{FWHM}/2$

$\lesssim 3.0$ kpc indicative of a highly structured eDIG morphology. These results suggest that the eDIG is often tied to the H II regions within the disk, providing support to the hypothesis that the dominant source of ionization of the eDIG originates in the disk (e.g., Domgörgen & Mathis 1994; Mathis 2000). This issue is discussed in more detail in §7 and Paper II.

6.2. *Deviation from Average Vertical Profile*

To further quantify the topology of the eDIG, the $1\text{-}\sigma$ deviation of the eDIG emission from the average vertical profile was calculated. First, the average vertical profile of the $\text{H}\alpha$ emission was determined by averaging over all (galactocentric) radii. This average vertical profile was then subtracted from the emission profile at each radius to look for deviations from the average. For this procedure, the vertical emission profile at a given radius was renormalized such that the integrated flux measured at each radius is equal to the integrated flux associated with the average emission profile. All of the data points were also Poisson-weighted in order to allow comparisons between galaxies of different brightnesses, and to reduce the impact of the bright eDIG emission near the disk relative to the emission at high $|z|$.

The $1\text{-}\sigma$ deviation derived from this analysis is a rough indicator of the level of fluctuations in the extraplanar emission. High deviations are expected in galaxies with filamentary morphologies, since bright knots or plumes of emission as well as regions void of eDIG differ greatly from the average extraplanar emission. A galaxy with widespread diffuse eDIG emission would yield a low $1\text{-}\sigma$ deviation since the extraplanar emission is more uniform across the halo.

The values of the $1\text{-}\sigma$ deviations are listed in Table 7. For most galaxies, the results here are consistent with our findings in §6.1. Galaxies which show large $1\text{-}\sigma$ deviations also demonstrate a high level of correlation between disk and halo emission and sharp peaks in their correlation plots, reinforcing the conclusion that they exhibit structured morphology. Prime examples include the southeast side of NGC 2820 and the northern side of NGC 3044 (especially in the CTIO image). Galaxies with structured morphologies (based on the $1\text{-}\sigma$ deviations listed in Table 7) also appear to have greater eDIG masses (P[null] value ~ 0.01). Other interesting correlations are discussed in the next section.

7. THE INFLUENCE OF THE HOST GALAXY ON THE EDIG

Results from §5 and §6 indicate that the galaxies in our sample show a broad range in eDIG properties ($\text{H}\alpha$ luminosity, midplane emission measure and electron density, scale height, mass, and $1\text{-}\sigma$ deviation from exponential fit). To gain insight into the origin and possible sources of energy and ionization of the eDIG, it is important to find out if these quantities depend on the properties of the host galaxies. To address this issue, the properties of the eDIG listed in Tables 4 and 6 are compared with the host galaxy properties listed in Table 1. The results of these comparisons are listed in Table 8. A least-squares linear fit analysis is conducted for each data set, and the Pearson correlation coefficient r for the fit is computed as well as the Pearson's probability (P[null] value) of zero correlation. A correlation coefficient $r = 1.0$ denotes a perfect correlation, and a P[null] value less than ~ 0.01 indicates a significant correlation. To examine the impact of possible biases associated with distance and inclination, the least-squares linear fit analysis was conducted twice: once for the entire sample and another time

for a subset of 10 objects that excludes NGC 55 and the 6 galaxies in the sample with $i < 85^\circ$ (Table 8).

The lack of obvious correlation between inclination and any of the eDIG parameters (including the scale height) suggests that effects associated with low inclination are fairly modest and do not bias the results of our study. Distance biases are, however, present in our sample. The eDIG scale height shows a significant tendency to increase with increasing distance ($P[\text{null}] \approx 0.001$ for the entire sample and ~ 0.005 , when considering the subset of objects that excludes NGC 55 and the 6 low-inclination galaxies). This trend is attributed to the limited spatial resolution of the observations. The further away a galaxy lies, the harder it is to detect the extraplanar emission and to accurately measure the scale height. Our method may be overestimating this quantity in the more distant objects. Deep observations with higher spatial resolution will be needed to reduce this distance-related effect.

The strongest, physically meaningful correlation in the data set is found when comparing the infrared (or far-infrared) luminosities per unit disk area with the (one-sided) eDIG masses. These luminosities are an indicator of the amount of dust that is being heated by nearby stars in these galaxies, and therefore a good indicator of the star formation rate (e.g., Kennicutt 1998). Note the lack of a significant correlation between the $H\alpha$ and F/IR luminosities per unit area. This confirms that the $H\alpha$ luminosities are strongly affected by dust extinction in the disks and are not a good measure of the star formation rates in these highly inclined galaxies.

The strong correlation between F/IR luminosities per unit disk area and the eDIG masses indicates that the star formation rate per unit disk area influences the amount of eDIG. It may not be surprising *a posteriori* to find a strong correlation between these two quantities since a large star formation rate per unit disk area implies the presence of a large concentration of young, massive OB stars, and thus a large flux of UV photons which may be reaching and ionizing the extraplanar gas. The larger star formation rates in the infrared-bright disk galaxies also imply larger supernova rates and larger energy injection rates in the disk ISM, thus creating a greater number of superbubbles which expand and ultimately clear pathways for the gas and ionizing photons to escape into the halo (e.g., ‘‘porosity’’ parameter of Heiles 1990). This is not the first time that a correlation has been suggested to exist between the eDIG properties and the star formation rate (e.g., Dettmar 1992; Rand, Kulkarni, & Hester 1992; Veilleux et al. 1995), but the size of the current galaxy sample allows us to put this correlation on a more solid statistical footing.

Interestingly, there is no evidence for a significant correlation (or anti-correlation) between the F/IR luminosities per unit disk area and the midplane emission ($P[\text{null}] = 0.024$ and 0.030 when considering the entire sample) or scale height of the eDIG ($P[\text{null}] = 0.14$ and 0.19). This is perhaps surprising since the F/IR luminosity per unit disk area is a direct measure of the rate at which energy is injected into the disk (the greater the star formation rate, the greater the number of supernovae events per year, and the greater the flow of energy into the disk and halo), and numerical simulations predict that the eDIG layers reach larger scale heights and become more tenuous as the injected energy rate is increased (e.g., Rosen & Bregman 1995; de Avillez & Berry 2001). This comparison with the models assumes that the conditions in the disk ISM are the same for all of the galaxies in the sample, but this is almost certainly not be

the case. The predicted correlations may be masked by large galaxy-to-galaxy variations in the properties of the disk ISM (e.g., mass, density, clumpiness, etc). This may also explain the lack of any obvious correlation between the eDIG topology (as measured by the peak correlation coefficients of Table 6 or the $1-\sigma$ deviations listed in Table 7) and the F/IR luminosities per unit disk area.

8. SUMMARY

The present paper reports the results from a deep $H\alpha$ imaging survey of 17 nearby, edge-on disk galaxies down to flux limits of several $\times 10^{-18}$ erg s^{-1} cm^{-2} arcsec $^{-2}$. These data are used to study the properties of the extraplanar diffuse ionized gas (eDIG) in these objects. The results from this analysis are then compared with the global properties of these galaxies to constrain the nature and origin of the eDIG. The main conclusions of this study are as follows:

- All but one galaxy in the sample exhibit eDIG. The contribution of the eDIG to the total $H\alpha$ luminosity is fairly constant with an average value of $12 \pm 4\%$.
- The scale height of the eDIG derived from a two-exponential fit ranges from 0.4 kpc to 17.9 kpc, with an average of 4.3 kpc. This average value is noticeably larger than the eDIG scale height in our Galaxy and other galaxies. This difference in scale height is probably due to our two-exponential fitting method and to the fainter flux levels reached by our observations.
- The midplane electron densities of the eDIG based on the $H\alpha$ intensities at $|z| = 0$ derived from the two-exponential fits of the entire sample range from 0.020 cm^{-3} to 0.26 cm^{-3} , with an average value of 0.11 cm^{-3} . These numbers assume a constant filling factor with heights of 0.2, as determined in the midplane of our Galaxy (Reynolds 1990), and use a constant pathlength through the disk of $l = 5$ kpc (Veilleux et al. 1995). Using these electron densities, we find that the total (two-sided) extraplanar ionized masses range from $1.4 \times 10^7 M_\odot$ to $2.4 \times 10^8 M_\odot$, with an average value of $1.2 \times 10^8 M_\odot$. Under these same assumptions, the recombination rate required to keep the eDIG ionized ranges from 0.44 to $13 \times 10^7 s^{-1}$ per cm^{-2} of the disk, equivalent to 10% to 325% of the Galactic value.
- The lack of obvious correlation between inclination and any of the eDIG parameters indicates that inclination biases do not significantly affect the results of our study. The limited spatial resolution of our observations and broad range in distance of our sample galaxies appears to introduce a distance-related bias on the eDIG scale height. Our method may be overestimating this quantity in the more distant objects of our sample.
- A quantitative analysis of the topology of the eDIG indicates that about half of the galaxies in the sample have a highly structured eDIG morphology. There is often a correlation between the intensity of the eDIG emission and the locations of the H II regions in the disk, providing support to the hypothesis that the predominant source of ionization of the eDIG is photoionization from OB stars located in the H II regions.

- Comparisons between the various properties of the eDIG and the global properties of the host galaxies indicate that the strongest, physically meaningful correlation is seen between the F/IR luminosities per unit disk area (basically a measure of the star formation rate per unit disk area) and the extraplanar ionized mass, further supporting the existence of a strong connection between the eDIG and the disk of the galaxy. Contrary to model predictions, no significant correlation is seen between the midplane electron density or scale height of the eDIG and the infrared luminosity per unit disk area of the host galaxy. This apparent discrepancy may be due to large galaxy-to-galaxy variations in the properties of the disk ISM.
- [N II] $\lambda 6583/H\alpha$ ratio maps in 10 galaxies show (or, in some cases, confirm) the existence of vertical excitation gradients in six of them, and a general trend to detect larger [N II]/ $H\alpha$ ratios at lower $H\alpha$ surface brightnesses in two additional objects. The large ratios in the eDIG can generally be explained through photoionization by OB stars in the disk as long as one takes into account the multi-phase nature of the ISM, the possible depletion of certain gas-phase abundance of metals onto dust grains, and the absorption and hardening of the stellar radiation field as it propagates through the dusty disk. This issue is examined in more detail in Paper II, where long-slit spectra are used to deduce that hybrid models which combine photoionization by OB stars and another source of ionization such as photoionization by turbulent mixing layers or shocks provide a better fit to the line ratios in the eDIG.

The authors are indebted to the Time Allocation Committees of KPNO, CTIO, AAT, and WHT for their generous allocation of telescope time for this project. The authors wish to thank J. Bland-Hawthorn for countless discussions on the issues discussed in this paper, and for assistance in using the Taurus Tunable Filter for both the AAT and WHT observing runs. The authors thank the referee, René Walterbos, for several suggestions which significantly improved this paper, as well as Andrew Wilson, Stacy McGaugh, and Kim Weaver who read and commented on an early version of this paper. SV is indebted to the California Institute of Technology and the Observatories of the Carnegie Institution of Washington for their hospitality, and is grateful for partial support of this research by a Cottrell Scholarship awarded by the Research Corporation, NASA/LTSA grant NAG 56547, and NSF/CAREER grant AST-9874973. STM was also supported in part by NSF/CAREER grant AST-9874973. This work has made use of NASA's Astrophysics Data System Abstract Service and the NASA/IPAC Extragalactic Database (NED), which is operated by the Jet Propulsion Laboratory, California Institute of Technology, under contract with the National Aeronautics and Space Administration.

Appendix: Notes on Individual Objects

NGC 7817

The $H\alpha$ and [N II] $\lambda 6583$ images and corresponding [N II]/ $H\alpha$ ratio map of NGC 7817 obtained with the WHT/TTF are presented in Figure 1. An SABC galaxy with an inclination of 79° (the lowest in our survey), NGC 7817 presents a spiral arm pattern which is clearly visible in the images. A foreground star projected just south (and slightly west) of the nucleus is oversubtracted (resulting in the white “spot” noticeable on one of the spiral arms). Diffuse emission is visible between the bright H II regions in the disk of the galaxy, but little extraplanar emission is detected. While there may appear to be some faint eDIG on the northwest side of the galaxy ($EM \sim 5 \text{ pc cm}^{-6}$), the modest inclination of this galaxy makes it difficult to determine whether this material is indeed high $|z|$ gas rather than emission at moderately large galactocentric radius. The [N II]/ $H\alpha$ ratios of the diffuse gas are noticeably larger than in the bright H II regions.

An $H\alpha$ luminosity/ D_{25}^2 of $5.0 \times 10^{37} \text{ erg s}^{-1} \text{ kpc}^{-2}$ is derived from the data, $\sim 11\%$ of which is attributed to eDIG. The extraplanar gas has a scale height of $\sim 1.7 \text{ kpc}$ on the northwest side and 1.9 kpc on the southeast side, and a total eDIG mass of $\sim 1.1 \times 10^8 M_\odot$. The extraplanar and disk emission components are strongly correlated, but the difficulty in separating the disk from the halo makes this result uncertain. The rather large $1-\sigma$ deviation of the northwest halo gas may be due in part to the low inclination of this galaxy rather than filaments or plumes extending up into the halo.

NGC 55

NGC 55 is nearest galaxy in our sample. It was observed at both CTIO and AAT, but the AAT observation covers a smaller portion of the galaxy. The $H\alpha + [\text{N II}]$ image obtained at CTIO and the separate $H\alpha$ and [N II] images obtained with the TTF on the AAT are shown in Figure 2, along with a [N II]/ $H\alpha$ ratio map. A number of arcs and plumes are detected in the AAT image. These data are also affected by reflective ghosts which complicate the interpretation of the ratio map (the arc-like feature of large [N II]/ $H\alpha$ across the map is an artifact of these ghosts). While the resolution of the CTIO image is not as high, this image does show the presence of a diffuse gas layer ($EM = 2 - 10 \text{ pc cm}^{-6}$) which extends out about 500 pc from the center of the galaxy, over a radial distance of $\sim 2 \text{ kpc}$ (in roughly the same region mapped by the AAT observations).

The CTIO image was corrected for [N II] contamination as detailed in §5.1. An $H\alpha$ luminosity/ D_{25}^2 of $3.9 \times 10^{37} \text{ erg s}^{-1} \text{ kpc}^{-2}$ is derived from this image, $\sim 5\%$ of which is attributed to eDIG. The scale height of the extraplanar gas has a value of 0.37 kpc on the NE side and a value of 0.45 kpc on the SW side. The total extraplanar ionized mass is $4.9 \times 10^7 M_\odot$. In general, these are some of the lowest values measured for all of our galaxies. The disk and extraplanar emission components are not well correlated and the $1-\sigma$ deviation are fairly modest. This suggests that the widespread emission apparent in the $H\alpha$ image is not well correlated with the H II regions found in the disk of the galaxy. The proximity of this galaxy makes this lack of correlation particularly obvious.

NGC 55 has been imaged by Ferguson et al. (1996), Hoopes et al. (1996), and Otte & Dettmar (1999). Ferguson et al. detected a number of loops and chimneys in the halo of NGC 55, up to distances of $\sim 1.5 \text{ kpc}$ (many of which are apparent in our images), as well as a faint shell of emission at a height of 2.6 kpc (not detected in our CTIO image, and outside the field of view of the AAT image). They measured a total $H\alpha + [\text{N II}]$ luminosity of $2.0 \times 10^{40} \text{ erg s}^{-1}$ and a diffuse gas fraction of $17 \pm 3\%$ for the inner 5 kpc of the galaxy. Hoopes et al. measure an $H\alpha + [\text{N II}]$ luminosity of $2.6 \times 10^{40} \text{ erg s}^{-1}$ and a diffuse gas fraction of $\sim 35\%$. Our measure of the diffuse gas fraction agrees with that of Ferguson et al., but our measurement of the $H\alpha$ luminosity is lower than both sets of observations; the additional [N II] emission in the Hoopes et al. and Ferguson et al. measurements accounts for some of the discrepancy. The measurements of Otte & Dettmar ($8.58 \times 10^{39} \text{ erg s}^{-1}$, based on a distance to NGC 55 of 1.6 Mpc) are in closer agreement with ours. The excitation map shown in Fig. 2 confirms the trend of finding large [N II]/ $H\alpha$ ratios in features with low $H\alpha$ surface brightnesses seen in the long-slit spectra of Ferguson et al. and Otte & Dettmar.

NGC 891

The $H\alpha$ and [N II] images of NGC 891 obtained with the TTF on the WHT are presented in Figure 3. As mentioned in Table 4, our image of NGC 891 is contaminated by a few poorly subtracted foreground stars and reflective ghost images. Nevertheless, the data clearly show a dust lane which intersects the galaxy, and diffuse emission extending over a broad range of radii and up to heights on the order of 2 kpc .

The $H\alpha$ luminosity/ D_{25}^2 ratio for this galaxy is $\sim 1.1 \times 10^{37} \text{ erg s}^{-1} \text{ kpc}^{-2}$. A scale height of $\sim 1.0 \text{ kpc}$ was measured for both halos, slightly smaller than the value derived by Rand, Kulkarni, & Hester (1990; 1.2 kpc) using a disk + bulge + halo decomposition, but larger than the value obtained by Dettmar (1990; 0.5 kpc) using a one-exponential fit. The total ionized mass of extraplanar material is estimated at $1.4 \times 10^8 M_\odot$. Based on the portion of NGC 891 which we were able to analyze, we find little filamentary emission, but rather widespread, diffuse emission above the disk.

The line ratio map shown in Figure 3 is affected by reflective ghosts but clearly shows the presence of a vertical [N II]/ $H\alpha$ gradient in this object, in agreement with results of long-slit studies (e.g., Keppel et al. 1991; Dettmar & Schultz 1992; Rand 1998, 2000).

NGC 973

The $H\alpha + [\text{N II}]$ image of NGC 973 is presented in Figure 4. At a distance of 63 Mpc , this galaxy is the most distant in our sample, and so has the worst linear resolution. An extremely bright, foreground star (not shown) lies close to the NE side of the galaxy, making accurate sky subtraction in this region difficult. The residuals from another star located on the NE side of the galaxy are also visible. As a consequence, estimates for the “global” properties of NGC 973 exclude the northeasternmost portion of the galaxy. Extraplanar emission with an average $EM = 7 \text{ pc cm}^{-6}$ appears to extend from the nucleus to the SE halo of NGC 973.

The $H\alpha$ luminosity/ D_{25}^2 ratio for NGC 973 is $\sim 0.8 \times 10^{37}$ erg s $^{-1}$ kpc $^{-2}$, $\sim 16\%$ of which is attributed to extraplanar gas. A two-exponential fit was not possible for the SE halo of the galaxy, but a scale height of 5.0 kpc was measured for the NW halo; this number is uncertain because it relies on the detection of very faint emission. The total ionized mass of extraplanar material is only $3.9 \times 10^7 M_{\odot}$ and also quite uncertain. The disk and halo gas emission are strongly correlated and there is no suggestion of widespread, diffuse emission above the disk.

Pildis et al. (1994b) observed NGC 973, but were unable to detect any extraplanar emission down to a limit of 4.6×10^{-17} erg s $^{-1}$ cm $^{-2}$ arcsec $^{-2}$ (or ~ 5 x our detection limit).

NGC 1507

The WHT/TTF $H\alpha$ and [N II] images of NGC 1507 are presented in Figure 5. NGC 1507 is an SB(s)m galaxy with an inclination of 80° . Only a few individual H II regions are visible in this galaxy. Gas with an average EM ~ 20 pc cm $^{-6}$ appears to extend up to 1 kpc in height (beyond the H II regions) over a range of radii $R = 2 - 4$ kpc on the southern side of the galaxy.

A $H\alpha$ luminosity/ D_{25}^2 ratio of 39.8×10^{37} erg s $^{-1}$ kpc $^{-2}$ is derived from this image, $\sim 11\%$ of which is attributed to extraplanar gas. The extraplanar gas has a scale height of ~ 0.56 kpc on the west side and 0.73 kpc on the east side, and a total extraplanar ionized mass of $\sim 7.3 \times 10^7 M_{\odot}$. A rather strong correlation is found between the extraplanar and disk emission on the west side of the galaxy, and Figure 20 indicates that the western extraplanar emission appears to extend over $R = 1 - 3$ kpc in the southern portion of the galaxy.

Although a slight mismatch in the central wavelengths of the $H\alpha$ and [N II] images is causing an artificial radial gradient in the excitation map (Fig. 5), there is clear evidence for the [N II]/ $H\alpha$ ratios in this galaxy to be systematically larger outside of the bright H II regions and at large $|z|$.

ESO 362-11

$H\alpha$ and [N II] images of ESO 362-11 are shown in Figure 6 (the bright spot in the southern halo is the residuals from a bright foreground star). This Sbc galaxy was observed at the AAT with the TTF. A dust lane clearly bisects the nucleus of ESO 362-11, confirming its inclination angle of 90° .

A $H\alpha$ luminosity/ D_{25}^2 ratio of 0.8×10^{37} erg s $^{-1}$ kpc $^{-2}$ is derived from this image, only $\sim 3\%$ of which is attributed to extraplanar gas. The extraplanar gas has a scale height of ~ 6.8 kpc on the south side and 3.3 kpc on the north side, and a total extraplanar ionized mass of $\sim 1.2 \times 10^8 M_{\odot}$. A rather strong correlation is found between the disk and extraplanar emission on the south side of the galaxy, but there appears to be a significant radial shift of ~ 2 kpc. No obvious correlation is seen with the northern halo.

The ratio map, also shown in Figure 6, suggests the presence of a vertical [N II]/ $H\alpha$ gradient in this galaxy, although a slight mismatch in the central wavelengths of the $H\alpha$ and [N II] images is clearly causing an artificial radial gradient in the data.

NGC 2188

Figure 7 presents $H\alpha$, [N II], and [N II]/ $H\alpha$ maps of NGC 2188 obtained with the TTF on the AAT. The field of view prevents us from fully imaging this large galaxy; our results are based only on the portion of the galaxy within the field of view. A number of $H\alpha$ filaments and arcs of diffuse gas are apparent on the west side of this galaxy. Two prominent arcs of gas (with average EM ≈ 60 pc cm $^{-6}$) are clearly present in the western halo, roughly 4 kpc south of the nucleus. The emission measure of the filaments in the western halo is ~ 50 pc cm $^{-6}$ at a height of 800 pc.

Based on the portion of NGC 2188 that lies within the field of view of the TTF, the $H\alpha$ luminosity/ D_{25}^2 ratio is 9.8×10^{37} erg s $^{-1}$ kpc $^{-2}$, 13% of which is attributed to extraplanar gas. The scale height of the extraplanar gas is ~ 0.8 kpc for both the western and eastern halos, and the total extraplanar ionized mass (within the field of view) is $9.5 \times 10^7 M_{\odot}$. A strong correlation is found between the disk and extraplanar emission in NGC 2188, but the $1-\sigma$ deviations from the average vertical profile are small, suggesting that while there are a number of filaments and plumes in the halo of the galaxy, there is also a pervasive diffuse eDIG layer. This diffuse layer can be seen in Figure 7 extending into the halo out to about 1 kpc above the disk.

Domgörgen & Dettmar (1997) also imaged NGC 2188 in $H\alpha$ + [N II]. Our results closely match theirs. They measure an $H\alpha$ luminosity of 1.1×10^{40} erg s $^{-1}$, a value which matches ours within the errors of the measurements. They also detect a number of filamentary structures whose positions are highly correlated with H II regions located in the southern portion of the galaxy.

The [N II]/ $H\alpha$ ratio map is dominated by an artificial radial gradient due to a wavelength mismatch between the $H\alpha$ and [N II] images. Nevertheless a shallow vertical gradient appears to be present in this object, in general agreement with the spectroscopic results of Domgörgen & Dettmar.

NGC 2424

NGC 2424 is an SB(r)b galaxy with an inclination of 82° . This object was observed at both the KPNO and WHT, and both sets of images are shown in Figure 8. The better resolution of the WHT/TTF image allows us to trace the spiral arm pattern in the disk of the galaxy. The relatively large distance of NGC 2424 prevents us from resolving some of the H II regions in the disk; these unresolved H II regions may be mistaken for diffuse gas. Although the relatively small inclination and large distance of this galaxy make the analysis difficult, the WHT/TTF $H\alpha$ image seems to show an extended extraplanar layer with average EM = 7 pc cm $^{-6}$.

The $H\alpha$ luminosity/ D_{25}^2 ratio of this galaxy is $\sim 1.3 \times 10^{37}$ erg s $^{-1}$ kpc $^{-2}$, $\sim 13\%$ of which is attributed to extraplanar gas. The extraplanar gas has a scale height of ~ 10.8 kpc on the north side and 5.4 kpc on the south side (based on the WHT observations), and a total ionized mass of $\sim 2.2 \times 10^8 M_{\odot}$. These numbers are subject to large uncertainties. The relatively small $1-\sigma$ deviations and lack of significant correlation between extraplanar and disk emission suggest that a rather uniform layer of extraplanar gas is associated with NGC 2424.

The [N II]/ $H\alpha$ of NGC 2424 (Fig. 8) is unusual in that it does not show any obvious vertical gradient. The central region harbors [N II]/ $H\alpha$ ratios larger than unity.

ESO 209-9

The $H\alpha + [N II]$ image of ESO 209-9 is shown in Figure 9. Little $H\alpha$ emission is detected anywhere in the galaxy, let alone extended emission into the halo. This is the only galaxy in the sample with no obvious signs of extraplanar line emission. The modest flux limit ($\sim 2 \times 10^{-17} \text{ erg s}^{-1} \text{ cm}^{-2} \text{ arcsec}^{-2}$) and spatial resolution (in pc) may explain the apparent lack of eDIG in this object.

NGC 2820

NGC 2820 is part of an interacting group of galaxies which consists of NGC 2805 – NGC 2814 – NGC 2820 and Mrk 108. This is one of only two galaxies in our sample with obvious interacting companions (the other is NGC 3432). NGC 2820 was included in our study because radio continuum data by van der Hulst & Hummel (1985) show a thick disk of radio emission associated with this object, a possible indication that eDIG emission may also be present. While no emission has been detected connecting NGC 2805 to the other galaxies, van der Hulst & Hummel detected a radio continuum bridge between NGC 2820/Mrk 108 and NGC 2814. NGC 2820 is an SB(s)c galaxy with an inclination of 90° . The $H\alpha + [N II]$ image is presented in Figure 10. Two regions of extraplanar emission (about 2 kpc in height) are observed in the southeast halo. Fainter emission extending ~ 1 kpc up above the disk are also detected, one in the northwest halo at a distance of ~ 4.5 kpc southwest of the galactic center, the other in the southeast halo at a distance of ~ 5 kpc northeast of the center (both of which have average EM $\approx 8 \text{ pc cm}^{-6}$).

An $H\alpha$ luminosity/ D_{25}^2 of $2.0 \times 10^{37} \text{ erg s}^{-1} \text{ kpc}^{-2}$ is derived, 16% of which is attributed to extraplanar gas. A two-exponential fit does not reproduce adequately the extraplanar gas profile for the southeast halo, but the northwest halo gas has a scale height of 1.08 kpc and a total extraplanar ionized mass of $\sim 3.3 \times 10^7 M_\odot$ associated with it. The very strong correlation found between the southeast halo and disk gas (also evident in Fig. 20) indicates that the extraplanar emission is strongly tied to the H II regions in the disk of the galaxy. The large $1-\sigma$ deviations of the SE extraplanar gas indicates that the emission is not uniform across the galaxy, and confirms that the filamentary structure correlates strongly with the distribution of the H II regions in the disk.

NGC 3044

Like NGC 2820, NGC 3044 is an SB(s)c galaxy seen essentially edge-on (90°). NGC 3044 was observed with the WHT/TTF and at CTIO; the resulting $H\alpha$, $[N II]$, and $H\alpha + [N II]$ images are presented in Figure 11. Most remarkable in the WHT image is the arc of emission (with an EM $\sim 20 \text{ pc cm}^{-6}$) seen rising above the disk into the southern halo. Located about 1 kpc west of the nucleus, the arc is over 1 kpc in diameter and extends ~ 1.5 kpc into the halo. This is most likely an expanding superbubble seen in projection. Another arc of $H\alpha$ emission is detected ~ 7 kpc east of the nucleus with an EM of $20 - 35 \text{ pc cm}^{-6}$. This feature extends ~ 1 kpc into the halo. A more widespread layer of diffuse gas is also detected on both sides of the galaxy, extending upward to a height of ~ 3 kpc.

The total $H\alpha$ luminosity/ D_{25}^2 is $\sim 10 \times 10^{37} \text{ erg s}^{-1} \text{ kpc}^{-2}$, 16% of which is attributed to extraplanar gas. The scale height of the gas on the north side (4.7 kpc) is greater than that on the south side (2.6 kpc; based on the CTIO observations). The ionized mass associated with this extraplanar gas is $2.0 \times 10^8 M_\odot$, higher than most galaxies. The strong correlation between disk and north halo gas, but the small $1-\sigma$ deviation of the extraplanar emission from the average vertical profile (based on the WHT observations) suggest that the extensive extraplanar emission observed in the northern halo originates from H II regions in the disk of the galaxy, but is not concentrated over them (although the $H\alpha$ intensity is somewhat higher in these regions). The locations of the apparent bubbles extending into the southern halo do not appear to correlate with the H II regions in the disk of the galaxy, perhaps an indication that the H II regions in this region have had time to disappear since the supernovae events took place in the disk.

Rossa & Dettmar (2000) detect an extraplanar layer of DIG emission, but while we detect eDIG up to a height of 3 kpc, they only detect it up to a height of ~ 1 kpc. They also detect several plumes of emission. Rossa & Dettmar also detect the extended arc structure south of the disk of the galaxy. They measure an $H\alpha$ luminosity of $1.3 \times 10^{41} \text{ erg s}^{-1}$, slightly higher, but not significantly so, than ours. Collins et al. (2000) also observed NGC 3044 and detected similar features including an extensive extraplanar layer of DIG emission.

Mismatch in the central wavelengths of the $H\alpha$ and $[N II]$ images are causing a radial gradient in the ratio map. Nevertheless, a slight vertical gradient also appears to be present in $[N II]/H\alpha$, in agreement with the spectroscopic results of Otte & Dettmar (1999).

NGC 3432

The $H\alpha + [N II]$ image of NGC 3432, an SB(s)m galaxy with an inclination of 84° , is presented in Figure 12. Our analysis of the halo gas was complicated by the presence of three, very bright foreground stars located near NGC 3432 which did not subtract out very well. The regions contaminated by these stars were excluded from the calculations of the eDIG properties. Some eDIG is apparent over the inner 2 kpc of the galaxy, extending out about 1.5 kpc in height and ranging in EM from 2 to 10 pc cm^{-6} . A faint arc of gas (possibly a superbubble) with an average EM $\approx 10 \text{ pc cm}^{-6}$ is located ~ 3 kpc from the center of the galaxy, extending out into the NW halo. It is only ~ 500 pc in diameter but reaches a height of 1 kpc.

The derived $H\alpha$ luminosity/ D_{25}^2 is $8.6 \times 10^{37} \text{ erg s}^{-1} \text{ kpc}^{-2}$, only $\sim 7\%$ of which is attributed to extraplanar gas. The scale height of the gas is ~ 1.0 kpc on either side of the galaxy, and the ionized mass associated with this extraplanar gas is $5.5 \times 10^7 M_\odot$. The disk and halo components of NGC 3432 are not strongly correlated with each other. The relatively small $1-\sigma$ deviations indicate relatively smooth eDIG morphology.

English & Irwin (1997) observed NGC 3432 in $H\alpha$ and 20 cm radio continuum. They detect one extraplanar filament extending away from the galaxy (what we called in the first paragraph a “faint arc of gas”), but conclude that extraplanar emission detected in NGC 3432 is due to tidal interactions with UGC 5983 (at the time of observation, it was not apparent to us that NGC 3432 was an interacting galaxy, and so was included in our survey), and not indicative of any disk-halo interaction. Other than this one filament, they do not detect any other eDIG,

but point out that their $H\alpha$ observations were not done under photometric conditions and therefore were not very sensitive to faint diffuse emission.

NGC 4013

NGC 4013 is an Sb galaxy with an inclination angle of 90° , observed at the WHT with the TTF. The $H\alpha$ and [N II] images are shown in Figure 13. A dust lane is clearly present on the southwest side of the disk, and a poorly subtracted foreground star coincides with the position of the nucleus of the galaxy. Extraplanar emission is clearly detected at heights of ~ 2 kpc into the southeast halo above the nucleus ($EM = 45 \text{ pc cm}^{-6}$ at 1 kpc height) as well as into the northwest halo at ~ 2 kpc on the southwest side of the galaxy ($EM = 25 \text{ pc cm}^{-6}$ at 1 kpc height). A bright knot of $H\alpha$ emission is also detected in the northwest halo, at a galactocentric radius of 1 kpc on the northeast side.

The total $H\alpha$ luminosity/ D_{25}^2 for NGC 4013 is $3.2 \times 10^{37} \text{ erg s}^{-1} \text{ kpc}^{-2}$, only 6% of which is attributed to extraplanar gas. The scale height of the gas is ~ 1.5 kpc on the southeast side of the galaxy (the northwest side was poorly fit by a two-exponential function), and the total ionized mass associated with this extraplanar gas is $6.5 \times 10^7 M_\odot$. There is little or no correlation between the disk and halo gas, and no substantial deviation from the average extraplanar vertical profile with radius. The presence of the foreground star near the nucleus of the galaxy makes further analysis difficult.

NGC 4013 was also observed by Rand (1996). He detects four filaments on either side of the central region, forming an ‘‘H’’ structure which extends about 2.5 kpc into the halo. Rand also detects extraplanar emission on the northeast side, extending up about 2.5 kpc, as well as on the southwest side (but not as prominent). Interestingly, we also detect this less prominent emission on the southwest side, but not the brighter emission on the northeast side. Part of the apparent discrepancy comes from the fact that Rand’s data include a contribution from [N II] emission. The [N II] image and [N II]/ $H\alpha$ map indicate that the [N II] emission is enhanced in this region (we also observed this galaxy spectroscopically, and confirm that $[N II]/H\alpha \approx 1.5$ at $|z| \sim 1$ kpc; see Paper II). The ratio map also shows a strong vertical gradient. The [N II] $\lambda 6583/H\alpha$ ratios are H II region-like in the disk but reach values close to unity at $|z| \approx 1$ kpc.

NGC 4197

NGC 4197 is an Sc galaxy at an inclination of 79° ; the $H\alpha + [N II]$ image is shown in Figure 14. The relatively small inclination of this object makes it possible to trace the general spiral arm pattern in the disk of the galaxy. A few bright foreground stars are poorly subtracted, but only the one near the northeast edge of the galaxy is close enough in apparent position to affect our results. Two faint plumes ($EM \sim 5 \text{ pc cm}^{-6}$) are visible, both extending upward about 1 kpc in the southeast halo of the galaxy (one near the center of the galaxy; the other out at ~ 1 kpc).

We derive an $H\alpha$ luminosity/ D_{25}^2 of $4.8 \times 10^{37} \text{ erg s}^{-1} \text{ kpc}^{-2}$, $\sim 13\%$ of which is attributed to extraplanar gas. The extraplanar gas has a scale height of ~ 4.9 kpc and a total extraplanar ionized mass of $\sim 1.0 \times 10^8 M_\odot$. This scale height is uncertain as it is based on the detection of very faint emission. A strong

correlation between the SE halo emission and the disk suggests that the observed plumes originate from H II regions in the disk of the galaxy.

NGC 5529

A $H\alpha + [N II]$ image of NGC 5529 is shown in Figure 15. This Sc type galaxy is reported to be perfectly edge-on. It is also one of the farthest galaxies in our sample, so resolving H II regions is a challenge. The two bright knots 1–2 kpc west of the nucleus and 2–3 kpc above and below the disk of the galaxy are stars that did not completely subtract out. Given an inclination angle of 90° , there appears to be faint ($EM = 2 - 5 \text{ pc cm}^{-6}$), widespread extraplanar gas over the inner 10 kpc of the galaxy, but not nearly as bright as that which has been detected in NGC 891. No obvious plumes or filaments are detected.

The total $H\alpha$ luminosity/ D_{25}^2 is only $0.8 \times 10^{37} \text{ erg s}^{-1} \text{ kpc}^{-2}$, 16% of which is attributed to extraplanar gas. The scale height of the gas is greater on the southeast side (6.8 kpc) than that on the northwest side (4.5 kpc). But both of these numbers are uncertain because they are based on the detection of very faint emission. The total ionized mass associated with this extraplanar gas is $2.0 \times 10^8 M_\odot$, considerably higher than most galaxies (but then NGC 5529 is one of the larger galaxies in the sample with an optical radius of 78.8 kpc). Both the large deviations of the extraplanar gas from the average vertical profile and the strong correlations between disk and halo emission suggest that the northeast side of the galaxy is characterized by filamentary eDIG.

NGC 5965

At an inclination of 85° , NGC 5965 is similar to NGC 5529 in its measured properties. A faint spiral arm pattern is apparent in the $H\alpha + [N II]$ image (Figure 16). Very faint emission ($EM \sim 3 \text{ pc cm}^{-6}$) is detected extending out about 1–2 kpc from the bright H II regions, possibly indicating the presence of eDIG.

The total $H\alpha$ luminosity/ D_{25}^2 is $\sim 1.0 \times 10^{37} \text{ erg s}^{-1} \text{ kpc}^{-2}$, $\sim 16\%$ of which is attributed to extraplanar gas. The scale height of the faint extraplanar gas is ~ 11.6 kpc on the northwest side of the galaxy, and 6.5 kpc on the southeast side, and the total extraplanar ionized mass is $\sim 2.3 \times 10^8 M_\odot$. These numbers are uncertain because they are based on the detection of very faint emission. There is a strong correlation between the disk and halo emission on both sides of the galaxy, corresponding to the faint extraplanar emission observed over the inner regions of the galaxy.

ESO 240-11

Obtained at the AAT with the TTF, the $H\alpha$ and [N II] images of ESO 240-11 are presented in Figure 17. An inclination angle of 90° is reported for this galaxy, but looking at the inner region of the $H\alpha$ image, the disk emission does not run through the center of the bulge, suggesting that a slightly lower inclination (around 87°) is more accurate. A number of bright $H\alpha$ knots are visible slightly above the disk (with average $EM \approx 25 \text{ pc cm}^{-6}$), but if the inclination of the galaxy is not exactly 90° , given the rather large size of the galaxy, most if not all of these could very well be H II regions located in the disk of the galaxy at moderately large galactocentric radii. In between

these regions, though, is faint $H\alpha$ emission ($EM = 4 - 10 \text{ pc cm}^{-6}$), some of which appears to extend out into the halo of the galaxy.

The $H\alpha$ luminosity/ D_{25}^2 ratio in this galaxy is $\sim 2.2 \times 10^{37} \text{ erg s}^{-1} \text{ kpc}^{-2}$, 15% of which is attributed to extraplanar gas. A scale height (assuming a published inclination value of 90°) of 15.5 kpc was measured for the southwest halo, and a scale height of 17.9 kpc was measured for the northeast halo (the scale heights decrease only slightly if the inclination is 87° , but they are uncertain because they are based on the detection of very faint emission). The total ionized mass in the extraplanar material is $2.4 \times 10^8 M_\odot$. We find that the halo emission is highly correlated with the disk emission, suggesting a strong link between the extraplanar emission and the bright H II regions in the disk. The $[N \text{ II}]/H\alpha$ excitation map does not show any obvious vertical gradient, although a negative radial gradient may be present.

REFERENCES

- Aaronson, M., et al. 1982, *ApJS*, 50, 241
- Allen, R. J., Baldwin, J. E., & Sancisi, R. 1978, *A&A*, 62, 397
- Bland-Hawthorn, J., & Jones, D. H., 1998, *Publ. Astron. Soc. Australia*, 15, 44
- Bland-Hawthorn, J., Sokolowski, J., & Cecil, G., 1991, *PASP*, 103, 906
- Bottema, R., 1995, *A&A*, 295, 605
- Bregman, J. 1980, *ApJ*, 236, 577
- Bregman, J., & Houck, J., 1997, *ApJ*, 485, 159.
- Bregman, J., & Pildis, R., 1994, *ApJ*, 420, 570.
- Brinks, E., & Bajaja, E. 1986, *A&A*, 169, 14
- Cecil, G., Bland-Hawthorn, J., Veilleux, S., & Filippenko, A. V. 2001, *ApJ*, 555, 338
- Cecil, G., Bland-Hawthorn, J., & Veilleux, S. 2002, *ApJ*, 576, 745
- Chevalier, R. A., & Clegg, A. W. 1985, *Nature*, 317, 44
- Collins, J. A., & Rand, R. J. 2001, *ApJ*, 551, 57
- Collins, J. A., Rand, R. J., Duric, N., & Walterbos, R. A. M. 2000, *ApJ*, 536, 645
- Dahlem, M. 1997, *PASP*, 109, 1298
- Dahlem, M., Dettmar, R. -J., & Hummel, E. 1994, *A&A*, 290,384
- Dahlem, M., Lisenfeld, U., & Golla, G. 1995, *ApJ*, 444,119
- Dahlem, M., Heckman, T. M., Fabbiano, G., Lenhart, M. D., & Gilmore, D. 1996, *ApJ*, 461, 724
- Dahlem, M., Weaver, K. A., & Heckman, T. M. 1998, *ApJS*, 118, 401
- de Avillez, M. A. & Berry, D. L. 2001, *MNRAS*, 328, 708
- de Vaucouleurs, G., de Vaucouleurs, A., Corwin, H. G., Buta, r. J., Paturel, G., & Fouqué, P., 1991, *Third Catalogue of Bright Galaxies*, Springer, New York
- Dettmar, R. -J. 1990, *A&A*, 232, L15
- 1992, *Fund. Cosmic Physics*, 15, 143
- Dettmar, R. -J., & Schultz, H. 1992, *A&A*, 254, L25
- Deul, E. R., & den Hartog, R. H. 1990, *A&A*, 229, 362
- Domgörgen, H., & Dettmar, R.-J., 1997, *A&A*, 322, 391
- Donahue, M., Aldering, G., & Stocke, J.T. 1995, *ApJ*, 450, L45
- Ekers, R. D., & Sancisi, R. 1977, *A&A*, 54, 973
- Ellis, G. R. A. 1982, *Austr. Journal of Physics*, 35, 91
- English, J., & Irwin, J. A. 1997, *AJ*, 113, 2006
- Ferguson, A., Wyse, R., & Gallagher, J. 1996, *AJ*, 112, 2567
- Franx, M., & Illingworth, G. 1990, *ApJ*, 359, L41
- Golla, G., Dettmar, R.-J., & Domgörgen, H., 1996, *A&A*, 313, 439
- Golla, G., & Hummel, E. 1994, *A&A*, 284, 777
- Gourgoulhon E., Chamaroux, P., Fouqué, P., 1992, *A&A*, 255, 69
- Guélin, M. 1974, *Galactic Radio Astronomy: Proceedings from IAU Symposium #60*, Eds. F. J. Kerr and S. C. Simonson, Dordrecht-Holland; Boston: D. Reidel Pub. Co., p.51
- Guthrie, B. N. G., 1992, *A&AS*, 93, 255
- Habe, A., & Ikeuchi, S. 1980, *Progr. Theor. Phys.*, 64, 1995
- Haffner, L. M., Reynolds, R. J., & Tuftes, S. L. 1999, *ApJ*, 523, 223
- Heckman, T. M., Armus, L., & Miley, G. K. 1990, *ApJS*, 74, 833
- Heiles, C. 1979, *ApJ*, 229, 533
- 1984, *ApJS*, 55, 585
- 1990, *ApJ*, 354, 483
- Hodge, P., 1987, *PASP*, 99, 915
- Hoopes, C., Walterbos, R., Greenwalt, B., 1996, *AJ*, 112, 1429
- Hoopes, C. G., Walterbos, R. A. M., Rand, R. J. 1999, *ApJ*, 522, 669
- Houck, J. C., & Bregman, J. N. 1990, *ApJ*, 352, 506
- Howk, J. C., Savage, B. D. 2000, *AJ*, 119, 644
- Hummel, E., & van der Hulst, J. M. 1989, *A&AS* 81,51
- Hummel, E., & Dettmar, R. -J. 1990, *A&A*, 236, 33
- Hummel, E., Beck, R., & Dahlem, M. 1991a, *A&A*, 248, 23
- Hummel, E., Beck, R., & Dettmar, R. -J. 1991b, *A&AS* 87,309
- Hummel, E., Dahlem, M., van der Hulst, J. M., & Sukumar, S. 1991c, *A&A*, 246,10
- Irwin, J. A., & English, J., Sorathia, B. 1999, *AJ*, 117, 2102
- Jones, D. H., Shopbell, P. L., & Bland-Hawthorn, J. 2002, *MNRAS*, 329, 759
- Kahn, F. D. 1981, in *Investigating the Universe*, p. 1
- 1991, in *IAU Symp. 144, The Interstellar Disk-Halo Connection in Galaxies*, p. 1.
- Kennicutt, R. C. Jr., 1998, *ARA&A*, 36, 189
- Keppel, J. W., Dettmar, R.-J., Gallagher, J. S., & Roberts, M. S. 1991, *ApJ*, 374, 507
- Kim, S., Dopita, M. A., Staveley-Smith, L., & Bessell, M. S. 1999, *AJ*, 118, 2797
- Kulkarni, S. R., & Heiles, C. 1988, in *Galactic and Extragalactic Radioastronomy*, 2nd edition, eds. G. L. Verschuur, K. I. Kellermann, Springer, 95
- Landolt, A. U. 1992, *AJ*, 104, 340
- 1992, *AJ*, 104, 372
- Larson, R. B., & Dinerstein, H. L. 1975, *PASP*, 87, 911
- Martin, P. G. 1988, *ApJS*, 66, 125
- Massey, P., Strobel, K., Barnes, J. V., & Anderson, E., 1988, *ApJ*, 328, 315
- Mathis, J. S. 2000, *ApJ*, 544, 347
- Miller, S. T., & Veilleux, S. 2003, *ApJ*, 592, 000 (Paper II)
- Moshir, M., et al. 1995, *Explanatory Supplement to the IRAS Faint Source Survey*, Version 2, JPL D-10015 8/92 (Pasadena: JPL)(FSC)
- Norman, C. A., & Ikeuchi, S. 1989, *ApJ*, 345, 372
- Normandeau, M., Taylor, A. R., & Dewdney, P. E. 1996, *Nature*, 380, 687
- Otte, B., & Dettmar, R.-J., 1999, *A&A*, 343, 705
- Pildis, R. A., Bregman, J. N., & Schombert, J. M. 1994a, *ApJ* 423, 190
- 1994b, *ApJ* 427, 160
- Rand, R. J. 1996, *ApJ*, 462,712
- 1997, *ApJ*, 474, 129
- 1998, *ApJ*, 501, 137
- 2000, *ApJ*, 537, 13
- Rand, R. J., Kulkarni, S. R., & Hester, J. J. 1990, *ApJ*, 352,L1 (erratum: *ApJ*, 362, L35)
- 1992, *ApJ*, 396, 97
- Reynolds, R. J. 1980, *ApJ*, 236, 153
- 1984, *ApJ*, 282, 191
- 1985a, *ApJ*, 294, 256
- 1985b, *ApJ*, 298, L27
- 1988, *ApJ*, 333, 341
- 1989, *ApJ*, 339, L29
- 1990, in *IAU Symp. 139, The Galactic and Extragalactic Background Radiation*, eds. S. Bowyer & C. Leinert (Dordrecht: Kluwer), 157
- Reynolds, R. J., Roesler, F. L., & Scherb, F. 1974, *ApJ*, 192, L53
- 1977, *ApJ*, 211, 115
- Reynolds, R. J., Scherb, F., & Roesler, F. L. 1973, *ApJ*, 185, 869
- 1977, *ApJ*, 211, 115
- Reynolds, R. J., & Tuftes, S. L. 1995, *ApJ*, 439, L17
- Rosen, A. & Bregman, J. N. 1995, *ApJ*, 440, 634
- Rossa, J., & Dettmar, R.-J., 2000, *A&A*, 359, 433
- Salpeter, E. E. 1985, *Mitt. Astr. Ges.*, 63, 11
- Sanders, D. B., & Mirabel, I. F., 1996, *ARAA*, 34, 749
- Schiano, A. V. R. 1985, *ApJ*, 299, 24
- Scoville, N. Z., Polletta, M., Ewald, S., Stolovy, S. R., Thompson, R., & Rieke, M. 2001, *AJ*, 122, 3017
- Shapiro, P. R., & Benjamin, R. A. 1991, *PASP*, 103, 923
- Shapiro, P. R., & Field, G. B. 1976, *ApJ*, 205, 762
- Sokolowski, J., & Bland-Hawthorn, J. 1991, *PASP*, 103, 911
- Stone, R. P. S. 1977, *ApJ*, 218, 767
- Stone, R. P. S., & Baldwin, J. A. 1983, *MNRAS*, 204, 347
- Suchkov, A. A., et al. 1994, *ApJ*, 430, 511
- Swaters 1994, Undergraduate thesis, Univ. of Groningen
- Taylor, J. H., & Manchester, R. N. 1977, *ApJ*, 215, 885
- Tenorio-Tagle, G., & Bodenheimer, P. 1988, *ARAA*, 26, 45
- Tomisaka, K., & Ikeuchi, S. 1988, *ApJ*, 330, 695
- Tüllman, R., Dettmar, R.-J., Soida, M., Urbanik, M., & Rossa, J. 2000, *A&A*, 364, L36
- Tully, R. B., 1988, *Nearby Galaxies Catalog* (Cambridge: Cambridge University Press)
- Tully, R. B., Shaya, E. J., Pierce, M. J., 1992, *ApJS*, 80, 479
- Vader, P. 1986, *ApJ*, 305, 669
- Vallee, J. P., 1991, *A&A*, 251, 411
- van der Hulst, J. M. & Hummel, E. 1985, *A&A*, 150, L7
- Veilleux, S., Cecil, G., & Bland-Hawthorn, J. 1995, *ApJ*, 445, 152
- Veilleux, S., Cecil, G., Bland-Hawthorn, J., Tully, R. B., Filippenko, A. V., & Sargent, W. L. W., 1994, *ApJ*, 433,48.
- Wang, J., Heckman, T. M., & Lehnert, M. D. 1997, *ApJ*, 491, 114
- 1998, *ApJ*, 509, 93
- 1999, *ApJ*, 515, 97
- Wang, Q. D., Walterbos, R. A. M., Steakley, M., Norman, C., & Braun, R., 1995, *ApJ*, 439, 176.
- Yasuda, N., Fukugita, M., & Okamura, S., 1997, *ApJS*, 108, 417
- York, D. G. 1983, *ApJ*, 264, 172

FIG. 1.— Continuum-subtracted H α and [N II] λ 6583 images, and [N II] λ 6583/H α excitation map of NGC 7817 taken with the WHT/TTF. The bar in the upper-right hand corner of these images represents a distance of 1 kpc or $\sim 10''$. The cross in each panel indicates the position of the continuum nucleus. All of the images have been rotated counterclockwise through an angle of 45° . The directions in which each halo extends has been labeled (in this and all other images). Contours on the emission-line images represent flux levels of 5, 10, 20, 50, and 125×10^{-18} erg s $^{-1}$ cm $^{-2}$ arcsec $^{-2}$. The ratio map is on a linear intensity scale with contours at 0.2, 0.5, 1.0 and 1.4.

FIG. 2.— a) Continuum-subtracted H α + [N II] image of NGC 55 taken at CTIO, b) Continuum-subtracted H α and [N II] λ 6583 images, and [N II] λ 6583/H α excitation map of the central region of NGC 55 taken with the AAT/TTF. The bar in the upper-right hand corner of these images represents a distance of 1 kpc or $\sim 129''$. The cross in each panel indicates the position of the continuum nucleus. The images have been rotated clockwise through an angle of 18° . Contours represent flux levels of 10, 20, 40, 100, and 250×10^{-18} erg s $^{-1}$ cm $^{-2}$ arcsec $^{-2}$ in figure (a) and 5, 10, 20, 50, and 125×10^{-18} erg s $^{-1}$ cm $^{-2}$ arcsec $^{-2}$ in figure (b). The ratio map is on a linear intensity scale with contours at 0.2, 0.5, 1.0 and 1.4.

FIG. 3.— Continuum-subtracted H α and [N II] λ 6583 images, and [N II] λ 6583/H α excitation map of NGC 891 taken with the WHT/TTF. The bar in the upper-right hand corner of these images represents a distance of 1 kpc or $\sim 21''$. The cross in each panel indicates the position of the continuum nucleus. The images have been rotated counterclockwise through an angle of 68° . Contours on the emission-line images represent flux levels of 8, 16, 32, 80, and 200×10^{-18} erg s $^{-1}$ cm $^{-2}$ arcsec $^{-2}$. The ratio map is on a linear intensity scale with contours at 0.2, 0.5, 1.0 and 1.4.

FIG. 4.— Continuum-subtracted H α + [N II] image of NGC 973 taken at KPNO. The bar in the upper-right hand corner of this image represents a distance of 1 kpc or $\sim 3''$. The cross indicates the position of the continuum nucleus. The image has been rotated counterclockwise through an angle of 132° . Contours represent flux levels of 10, 20, 40, 100, and 250×10^{-18} erg s $^{-1}$ cm $^{-2}$ arcsec $^{-2}$.

FIG. 5.— Continuum-subtracted H α and [N II] λ 6583 images, and [N II] λ 6583/H α excitation map of NGC 1507 taken with the WHT/TTF. The bar in the upper-right hand corner of these images represents a distance of 1 kpc or $\sim 19''$. The cross in each panel indicates the position of the continuum nucleus. The images have been rotated counterclockwise through an angle of 79° . Contours on the emission-line images represent flux levels of 8, 16, 32, 80, and 200×10^{-18} erg s $^{-1}$ cm $^{-2}$ arcsec $^{-2}$. The ratio map is on a linear intensity scale with contours at 0.2, 0.5, 1.0 and 1.4.

FIG. 6.— Continuum-subtracted H α and [N II] λ 6583 images, and [N II] λ 6583/H α excitation map of ESO 362-11 taken with the AAT/TTF. The bar in the upper-right hand corner of these images represents a distance of 1 kpc or $\sim 13''$. The cross in each panel indicates the position of the continuum nucleus. The images have been rotated clockwise through an angle of 76° . Contours on the emission-line images represent flux levels of 0.8, 1.6, 3.2, 8, and 20×10^{-18} erg s $^{-1}$ cm $^{-2}$ arcsec $^{-2}$. The ratio map is on a linear intensity scale with contours at 0.2, 0.5, 1.0 and 1.4.

FIG. 7.— Continuum-subtracted H α and [N II] λ 6583 images, and [N II] λ 6583/H α excitation map of NGC 2188 taken with the AAT/TTF. The bar in the upper-right hand corner of these images represents a distance of 1 kpc or $\sim 13''$. The cross in each panel indicates the position of the continuum nucleus. The images have been rotated counterclockwise through an angle of 85° . Contours on the emission-line images represent flux levels of 3, 6, 12, 30, and 75×10^{-18} erg s $^{-1}$ cm $^{-2}$ arcsec $^{-2}$. The ratio map is on a linear intensity scale with contours at 0.2, 0.5, 1.0 and 1.4.

FIG. 8.— a) Continuum-subtracted H α + [N II] image of NGC 2424 taken at KPNO, b) Continuum-subtracted H α and [N II] λ 6583 images, and [N II] λ 6583/H α excitation map of NGC 2424 taken with the WHT/TTF. The bar in the upper-right hand corner of these images represents a distance of 1 kpc or $\sim 4''$. The cross in each panel indicates the position of the continuum nucleus. The images have been rotated counterclockwise through an angle of 9° . Contours represent flux levels of 8, 16, 32, 80, and 200×10^{-18} erg s $^{-1}$ cm $^{-2}$ arcsec $^{-2}$ in figure (a) and 6, 12, 24, 60, and 150×10^{-18} erg s $^{-1}$ cm $^{-2}$ arcsec $^{-2}$ in figure (b). The ratio map is on a linear intensity scale with contours at 0.2, 0.5, 1.0 and 1.4.

FIG. 9.— Continuum-subtracted H α + [N II] image of ESO 209-9 taken at CTIO. The bar in the upper-right hand corner of this image represents a distance of 1 kpc or $\sim 16''$. The cross indicates the position of the continuum nucleus. The image has been rotated counterclockwise through an angle of 64° . Contours represent flux levels of 10, 20, 40, 100, and 250×10^{-18} erg s $^{-1}$ cm $^{-2}$ arcsec $^{-2}$. This is the only galaxy in the sample with no obvious signs of eDIG.

FIG. 10.— Continuum-subtracted H α + [N II] image of NGC 2820 taken at KPNO. The bar in the upper-right hand corner of this image represents a distance of 1 kpc or $\sim 10''$. The cross indicates the position of the continuum nucleus. The image has been rotated counterclockwise through an angle of 31° . Contours represent flux levels of 15, 30, 60, 150, and 375×10^{-18} erg s $^{-1}$ cm $^{-2}$ arcsec $^{-2}$.

FIG. 11.— a) Continuum-subtracted H α + [N II] image of NGC 3044 taken at CTIO, b) Continuum-subtracted H α and [N II] λ 6583 images, and [N II] λ 6583/H α excitation map of NGC 3044 taken with the WHT/TTF. The bar in the upper-right hand corner of these images represents a distance of 1 kpc or $\sim 10''$. The cross in each panel indicates the position of the continuum nucleus. The images have been rotated clockwise through an angle of 13° . Contours represent flux levels of 10, 20, 40, 100, and 250×10^{-18} erg s $^{-1}$ cm $^{-2}$ arcsec $^{-2}$ in figure (a) and 5, 10, 20, 50, and 125×10^{-18} erg s $^{-1}$ cm $^{-2}$ arcsec $^{-2}$ in figure (b). The ratio map is on a linear intensity scale with contours at 0.2, 0.5, 1.0 and 1.4.

FIG. 12.— Continuum-subtracted H α + [N II] image of NGC 3432 taken at KPNO. The bar in the upper-right hand corner of this image represents a distance of 1 kpc or $\sim 26''$. The cross indicates the position of the continuum nucleus. The image has been rotated counterclockwise through an angle of 52° . Contours represent flux levels of 15, 30, 60, 150, and 375×10^{-18} erg s $^{-1}$ cm $^{-2}$ arcsec $^{-2}$.

FIG. 13.— Continuum-subtracted H α and [N II] λ 6583 images, and [N II] λ 6583/H α excitation map of NGC 4013 taken with the WHT/TTF. The bar in the upper-right hand corner of these images represents a distance of 1 kpc or $\sim 12''$. The cross in each panel indicates the position of the continuum nucleus. The images have been rotated counterclockwise through an angle of 24° . Contours on the emission-line images represent flux levels of 10, 20, 40, 100, and 250×10^{-18} erg s $^{-1}$ cm $^{-2}$ arcsec $^{-2}$. The ratio map is on a linear intensity scale with contours at 0.2, 0.5, 1.0 and 1.4.

FIG. 14.— Continuum-subtracted H α + [N II] image of NGC 4197 taken at KPNO. The bar in the upper-right hand corner of this image represents a distance of 1 kpc or $\sim 8''$. The cross indicates the position of the continuum nucleus. The image has been rotated counterclockwise through an angle of 54° . Contours represent flux levels of 15, 30, 60, 150, and 375×10^{-18} erg s $^{-1}$ cm $^{-2}$ arcsec $^{-2}$.

FIG. 15.— Continuum-subtracted H α + [N II] image of NGC 5529 taken at KPNO. The bar in the upper-right hand corner of this image represents a distance of 1 kpc or $\sim 4''$. The cross indicates the position of the continuum nucleus. The image has been rotated clockwise through an angle of 25° . Contours represent flux levels of 10, 20, 40, 100, and 250×10^{-18} erg s $^{-1}$ cm $^{-2}$ arcsec $^{-2}$.

FIG. 16.— Continuum-subtracted H α + [N II] image of NGC 5965 taken at KPNO. The bar in the upper-right hand corner of this image represents a distance of 1 kpc or $\sim 4''$. The cross indicates the position of the continuum nucleus. The image has been rotated clockwise through an angle of 37° . Contours represent flux levels of 10, 20, 40, 100, and 250×10^{-18} erg s $^{-1}$ cm $^{-2}$ arcsec $^{-2}$.

FIG. 17.— Continuum-subtracted H α and [N II] λ 6583 images, and [N II] λ 6583/H α excitation map of ESO 240-11 taken with the AAT/TTF. The bar in the upper-right hand corner of these images represents a distance of 1 kpc or $\sim 5''$. The cross in each panel indicates the position of the continuum nucleus. The images have been rotated counterclockwise through an angle of 141° . Contours on the emission-line images represent flux levels of 10 and 50×10^{-18} erg s $^{-1}$ cm $^{-2}$ arcsec $^{-2}$. The ratio map ranges from 0.3 (light grey areas) to about 0.9 – 1.0 (darker areas).

FIG. 18.— Distributions of the quantities derived from the narrow-band images. (a) total $H\alpha$ luminosity; (b) ratio of the total $H\alpha$ luminosity to the square of the galaxy diameter at $\mu_B = 25$ B mag arcsec⁻²; (c) diffuse gas fraction or the fraction of the $H\alpha$ -emitting material which is in the diffuse phase (see text for more detail); (d) $H\alpha$ luminosity from the eDIG; (e) fraction of the total $H\alpha$ luminosity which is produced by the eDIG; (f) scale height of the eDIG based on a two-exponential fit to the emission; (g) emission measure of the eDIG in the midplane derived from a two-exponential fit; (h) electron density of the eDIG in the midplane derived assuming a constant filling factor $f = 0.2$ and a line-of-sight length $l = 5$ kpc for all the galaxies; (i) one-sided ionized mass of the eDIG derived from the scale height and the midplane electron density; (j) peak value of the correlation at zero radial shift between the disk and the eDIG emission (see §6.1 for more detail); (k) $1-\sigma$ deviation of the eDIG from the average vertical profile (see §6.2 for more detail).

FIG. 19.— Exponential fits to the vertical profile of $H\alpha$ images. The dashed line represents a one-exponential fit while the dot-dash line represents a two-exponential fit. Both linear (top) and log (bottom) flux scales are shown for each galaxy.

FIG. 20.— (Top) The radial distribution of the extraplanar gas is compared to the radial distribution of the disk emission. The dark solid line represents the summed emission within the disk while the light solid line and the dashed line represent emission from both sides of the halo (as labeled in each graph). The halo emission has been scaled such that the maximum intensity has been set to unity and the relative intensities of both sides have been maintained. The disk emission has been scaled separately such that the maximum intensity of the disk has been set to unity. (Bottom) The panel on the left displays the correlation coefficient of the disk emission with one side of the halo emission while the panel on the right represents the correlation of the disk emission with the other side. A correlation value of 1 represents a perfect correlation while a value of -1 represents a perfect anti-correlation.

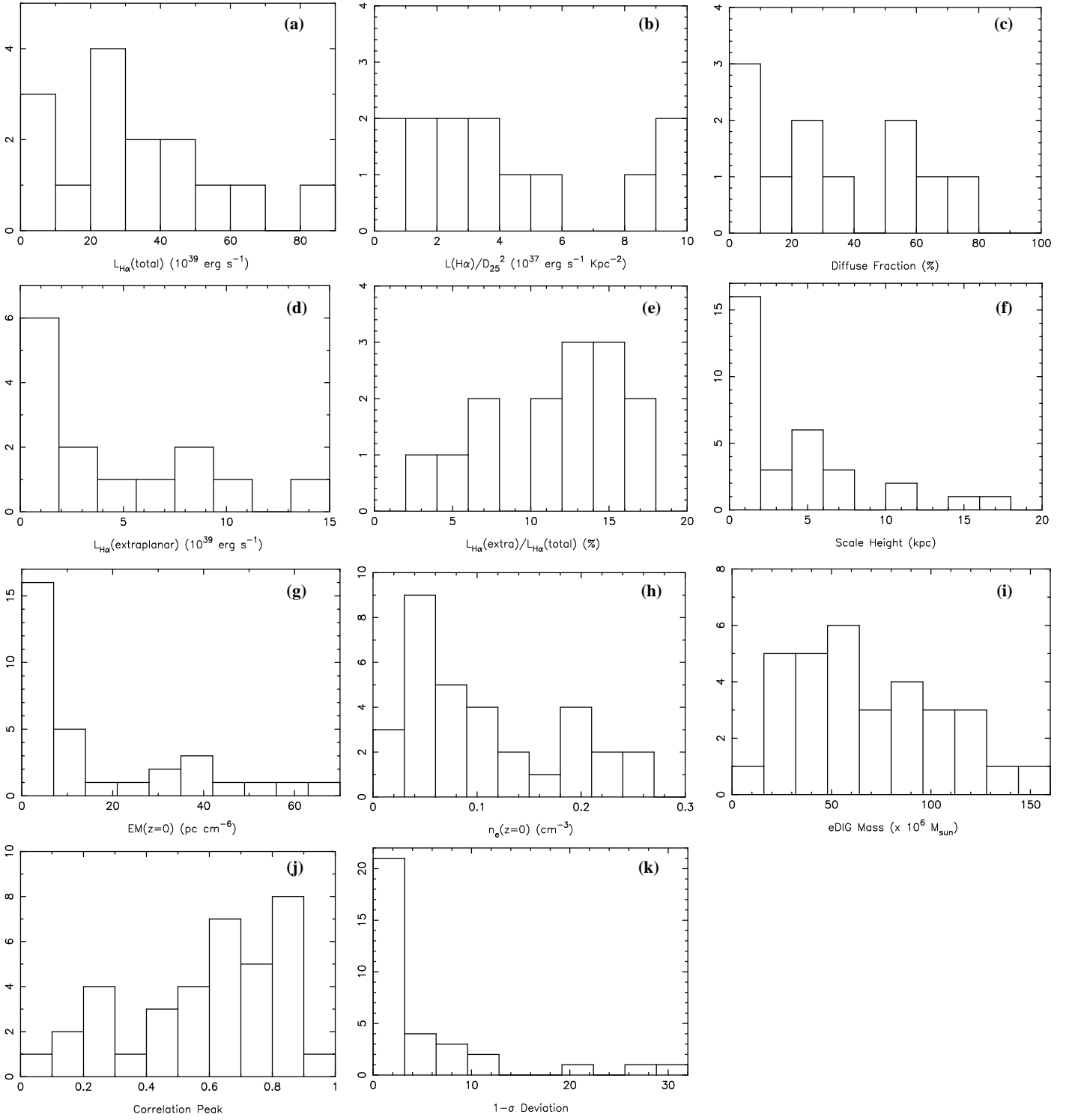


FIG. 18.—

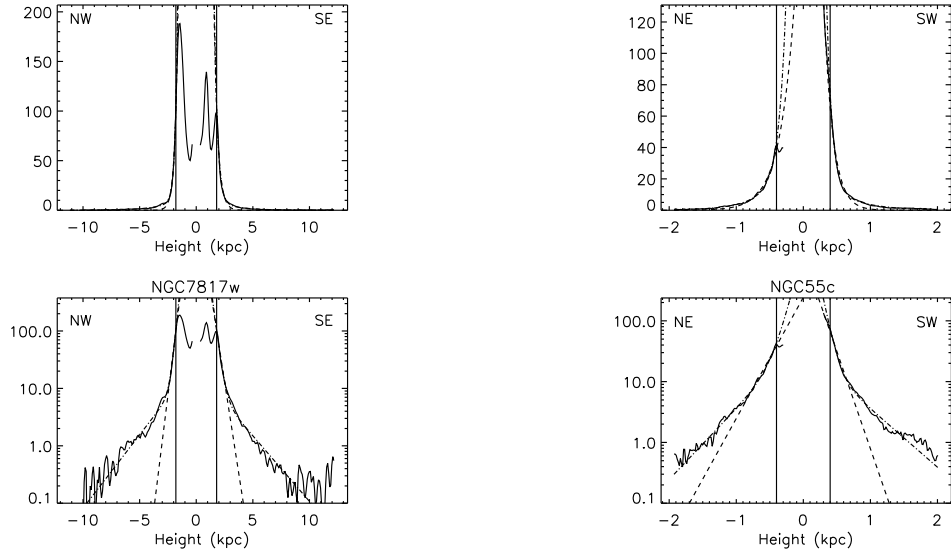


FIG. 19AB.—

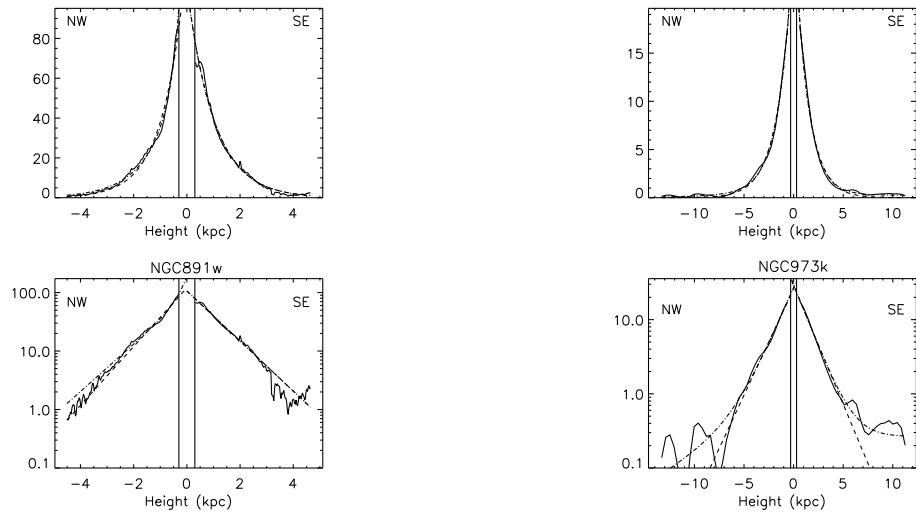


FIG. 19CD.— (Cont'd)

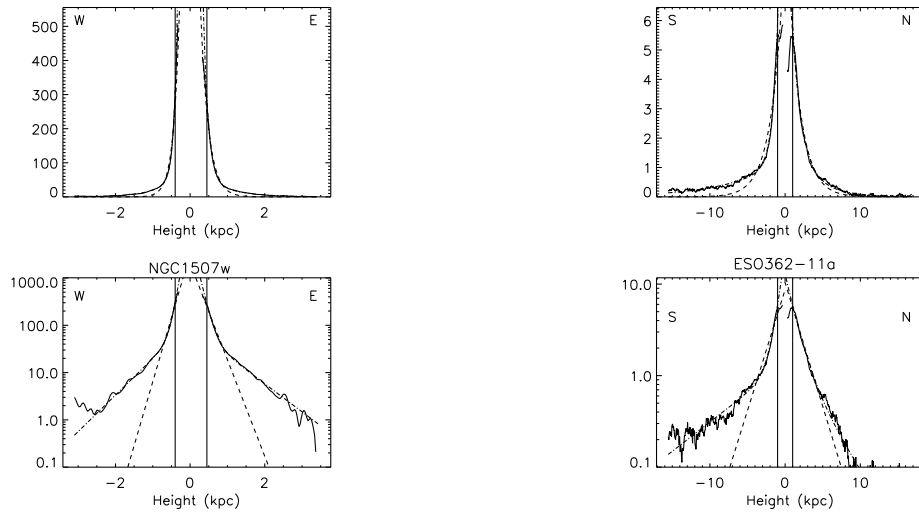


FIG. 19EF.— (Cont'd)

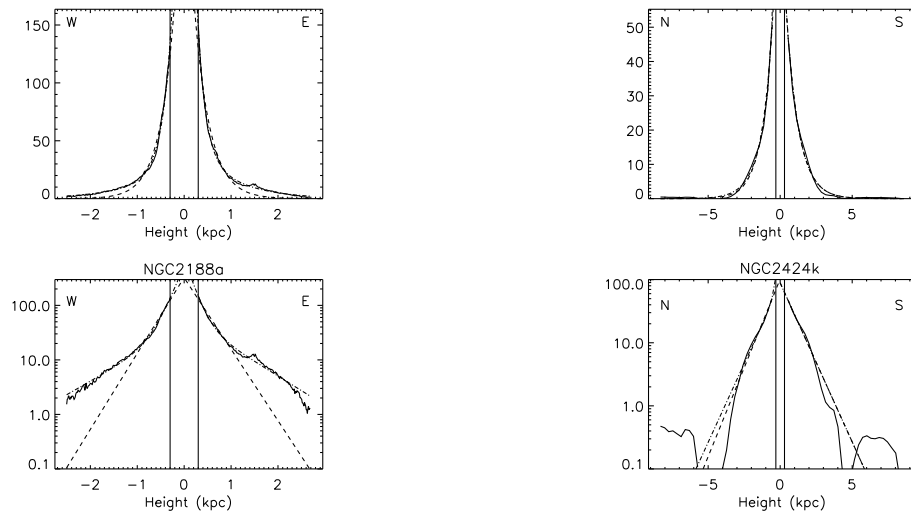


FIG. 19GH.— (Cont'd)

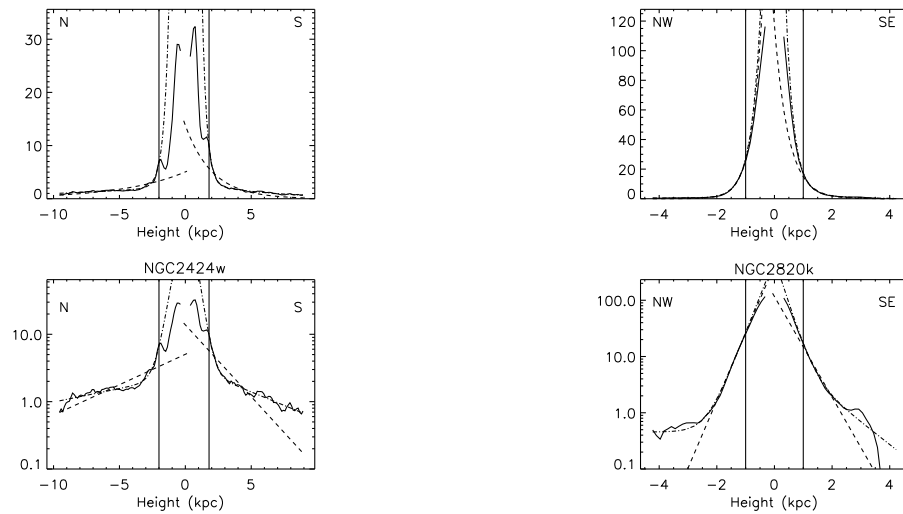


FIG. 19IJ.— (Cont'd)

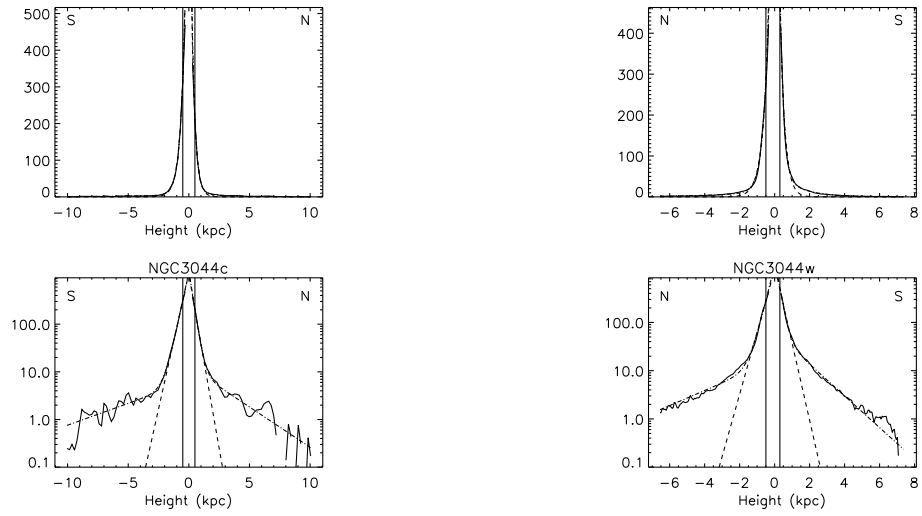


FIG. 19KL.— (Cont'd)

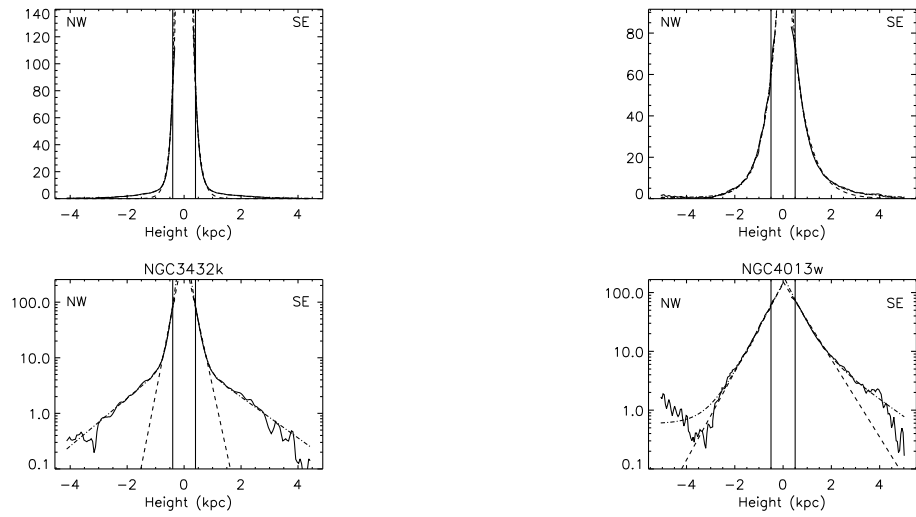


FIG. 19MN.— (Cont'd)

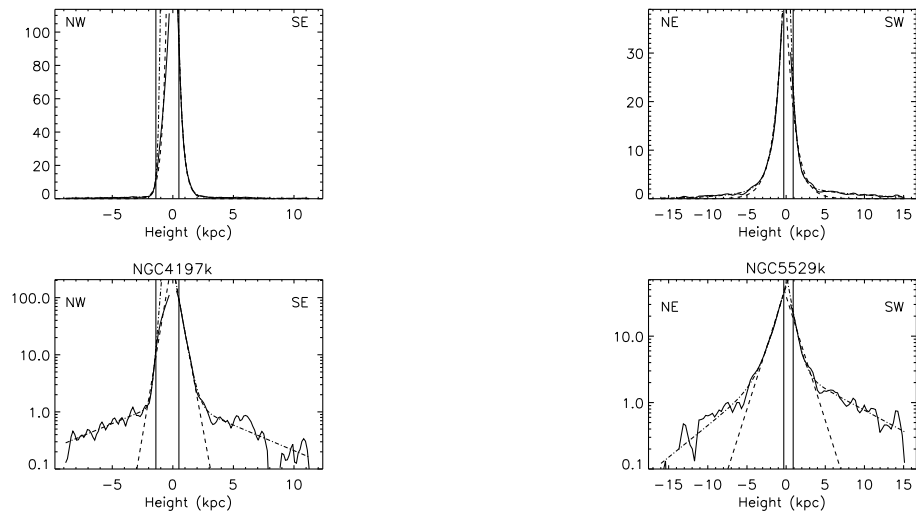


FIG. 19OP.— (Cont'd)

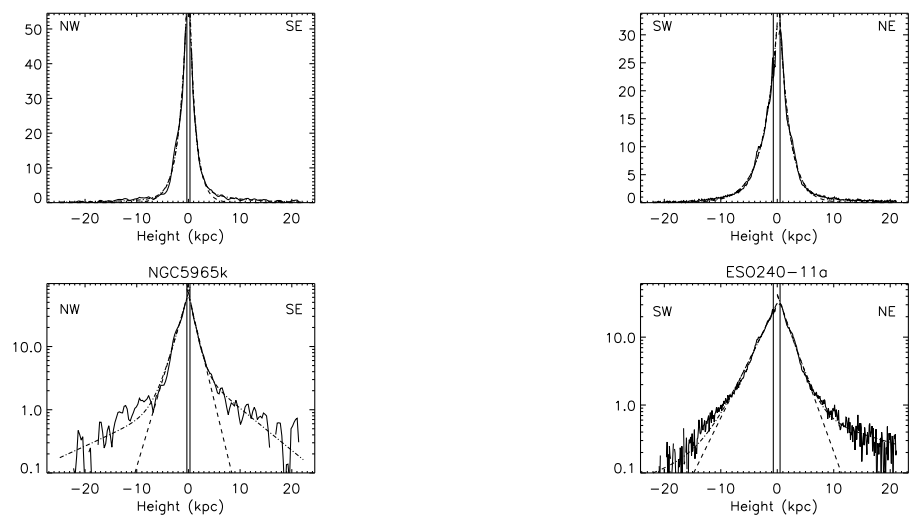


FIG. 19QR.— (Cont'd)

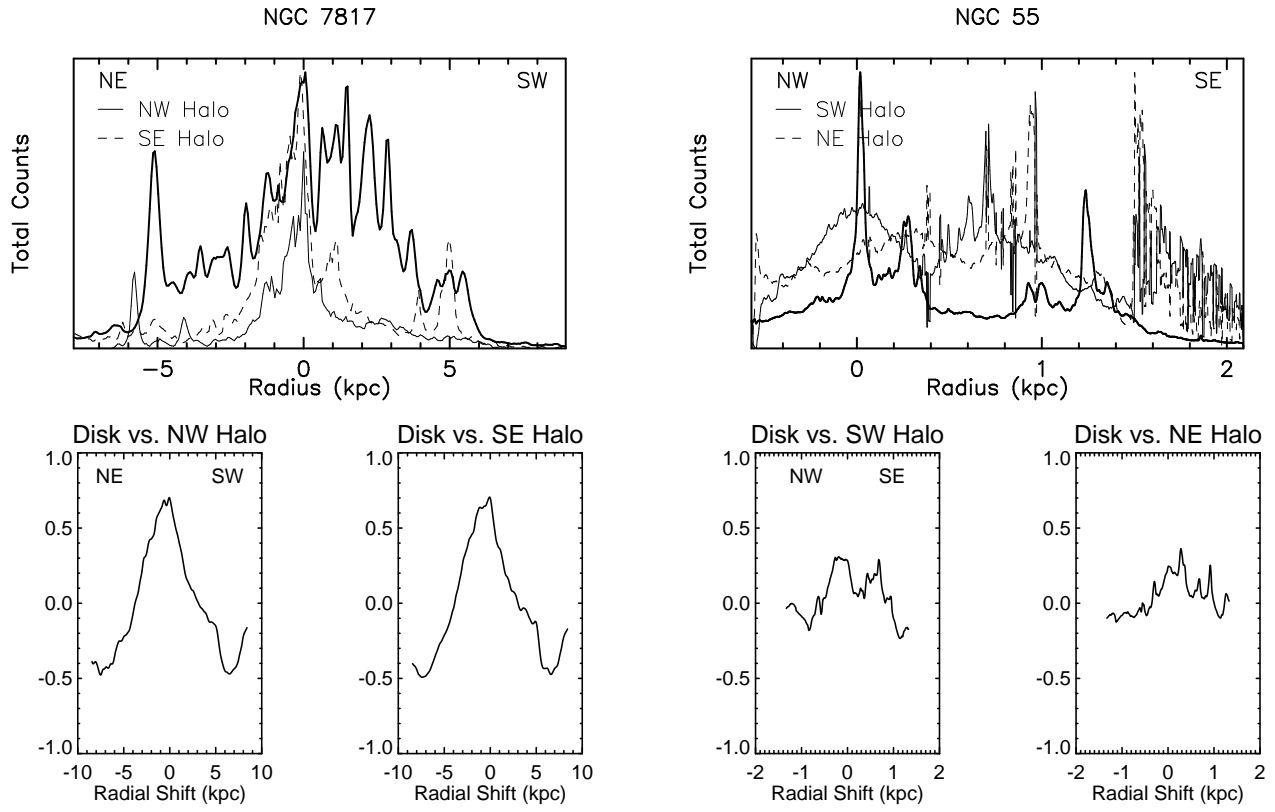


FIG. 20AB.—

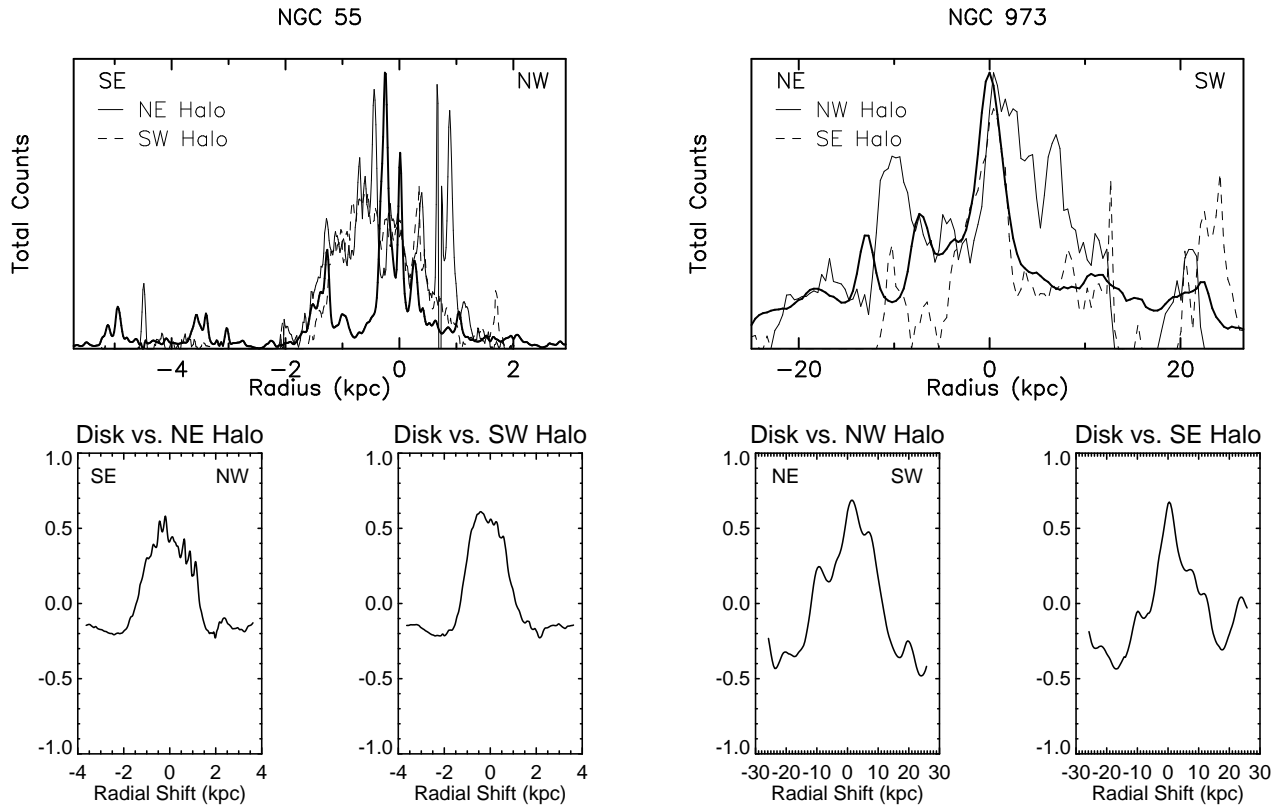


FIG. 20CD.— (Cont'd)

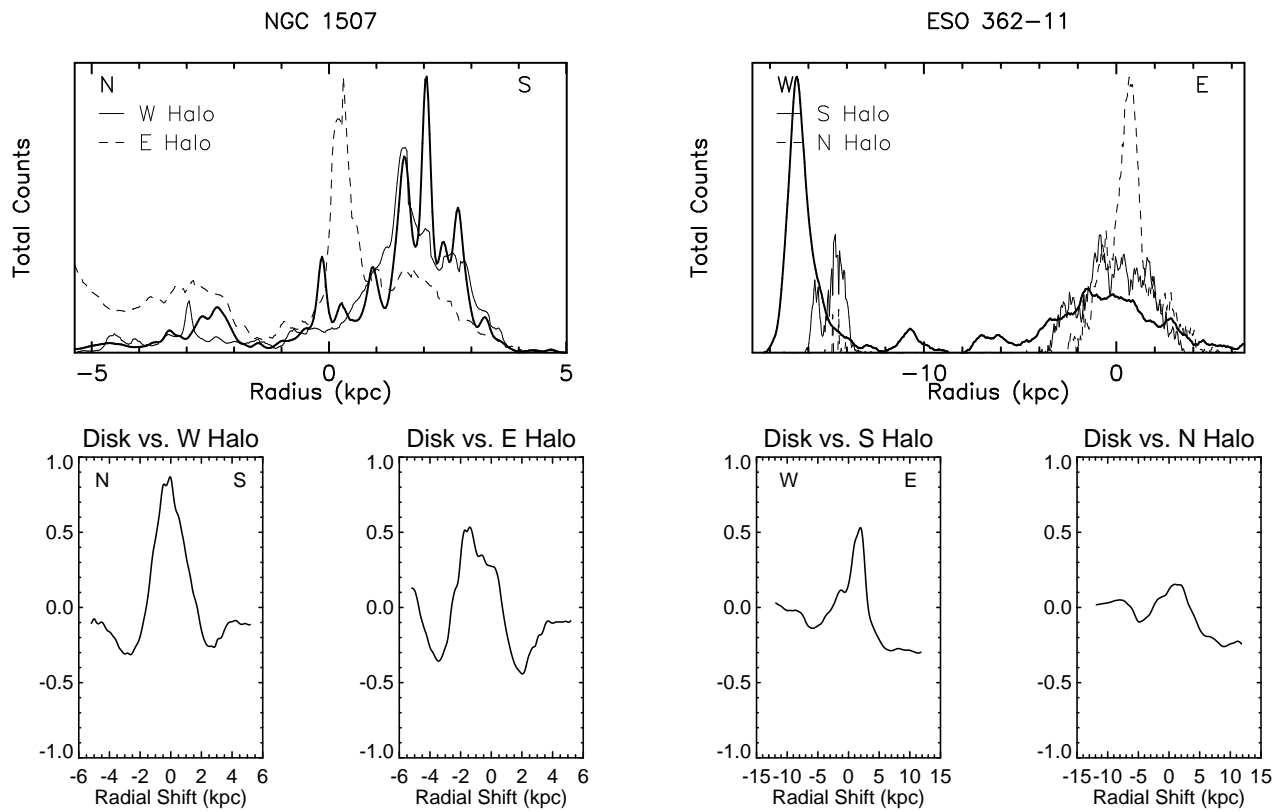


FIG. 20EF.— (Cont'd)

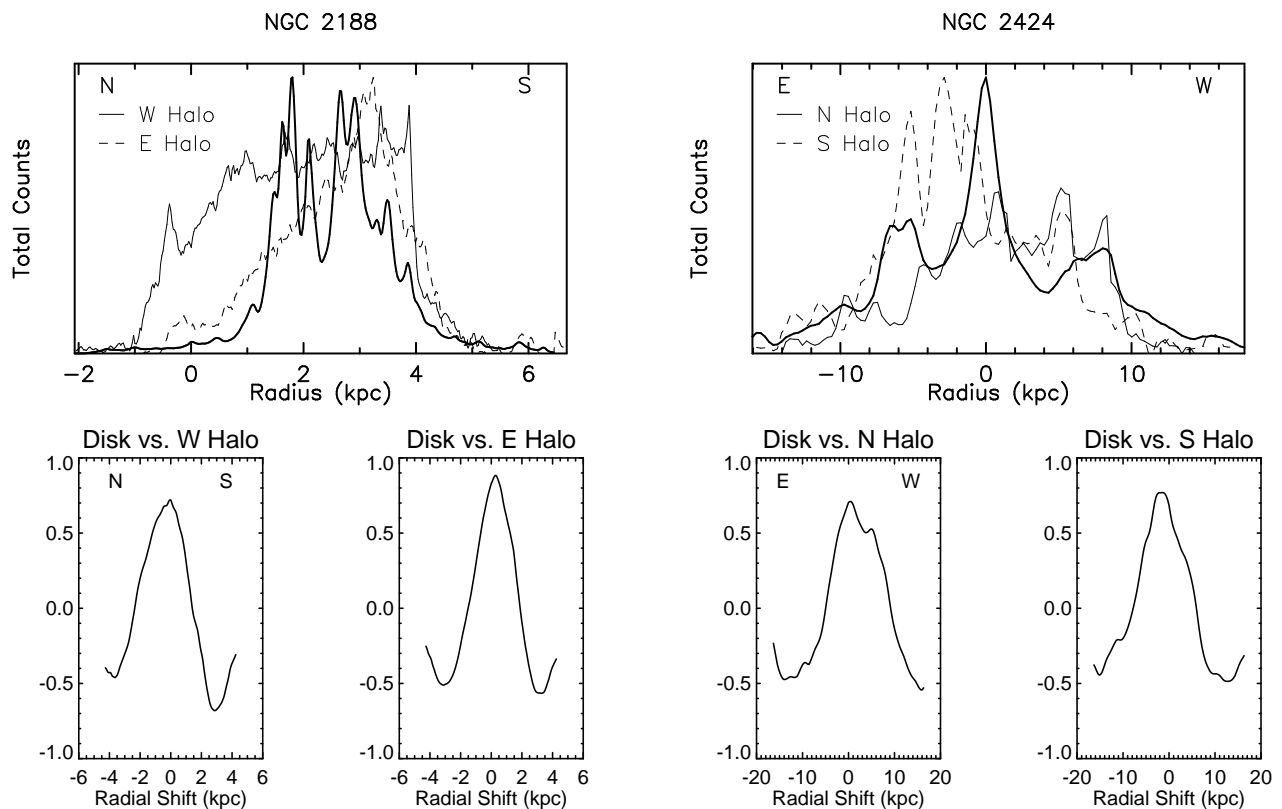


FIG. 20GH.— (Cont'd)

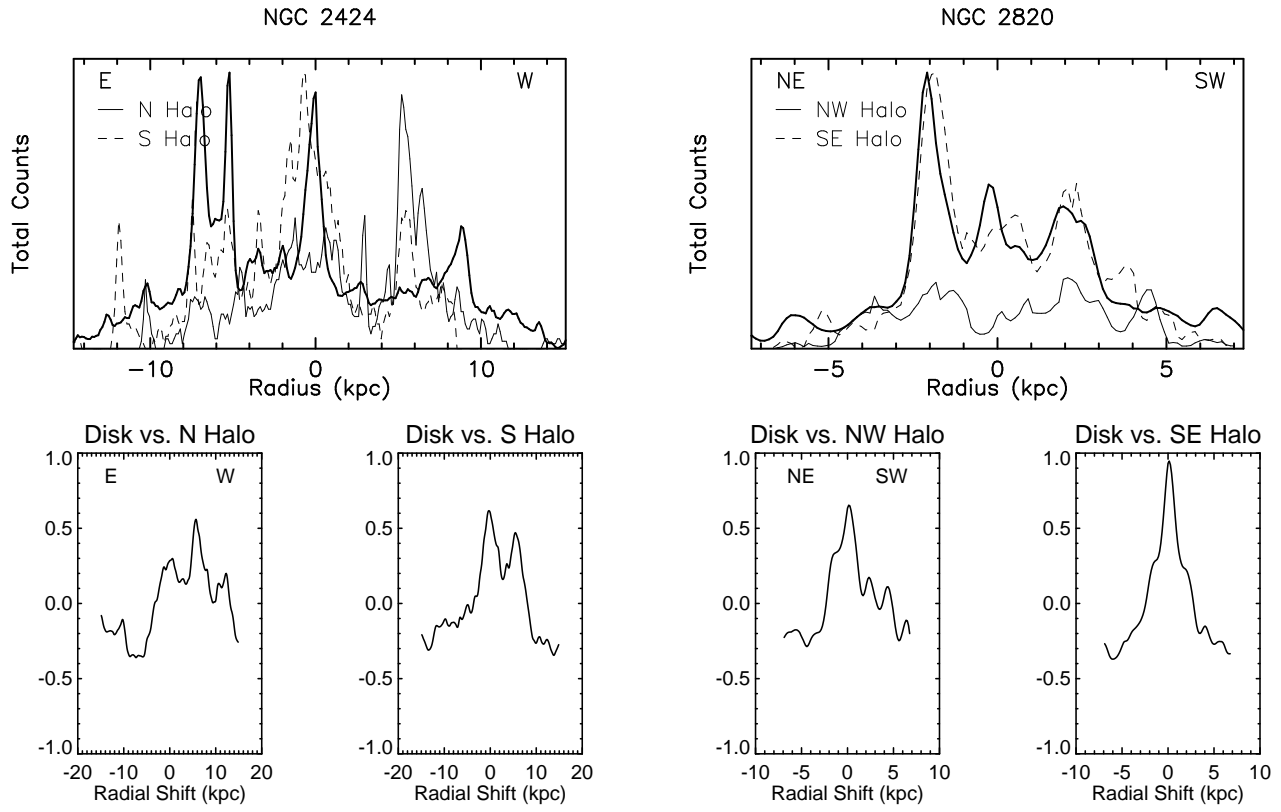


FIG. 20J.—(Cont'd)

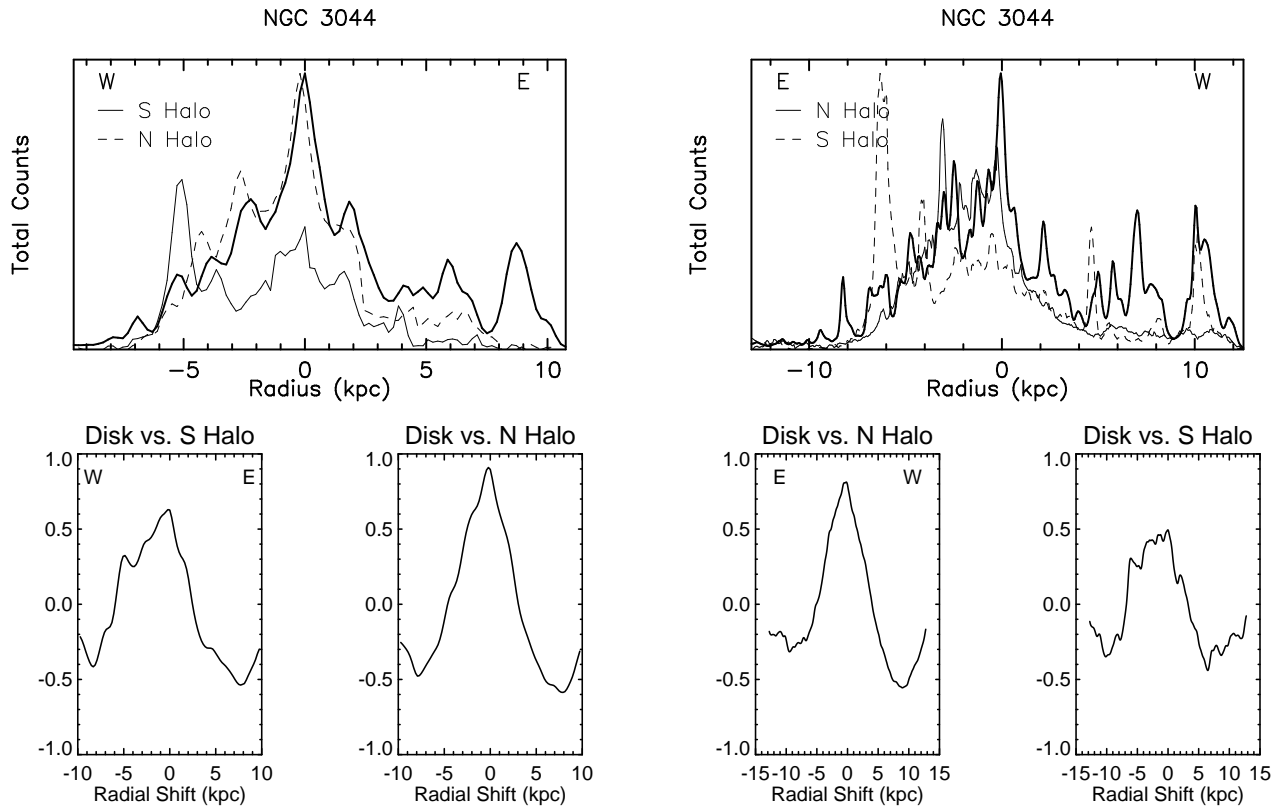


FIG. 20KL.—(Cont'd)

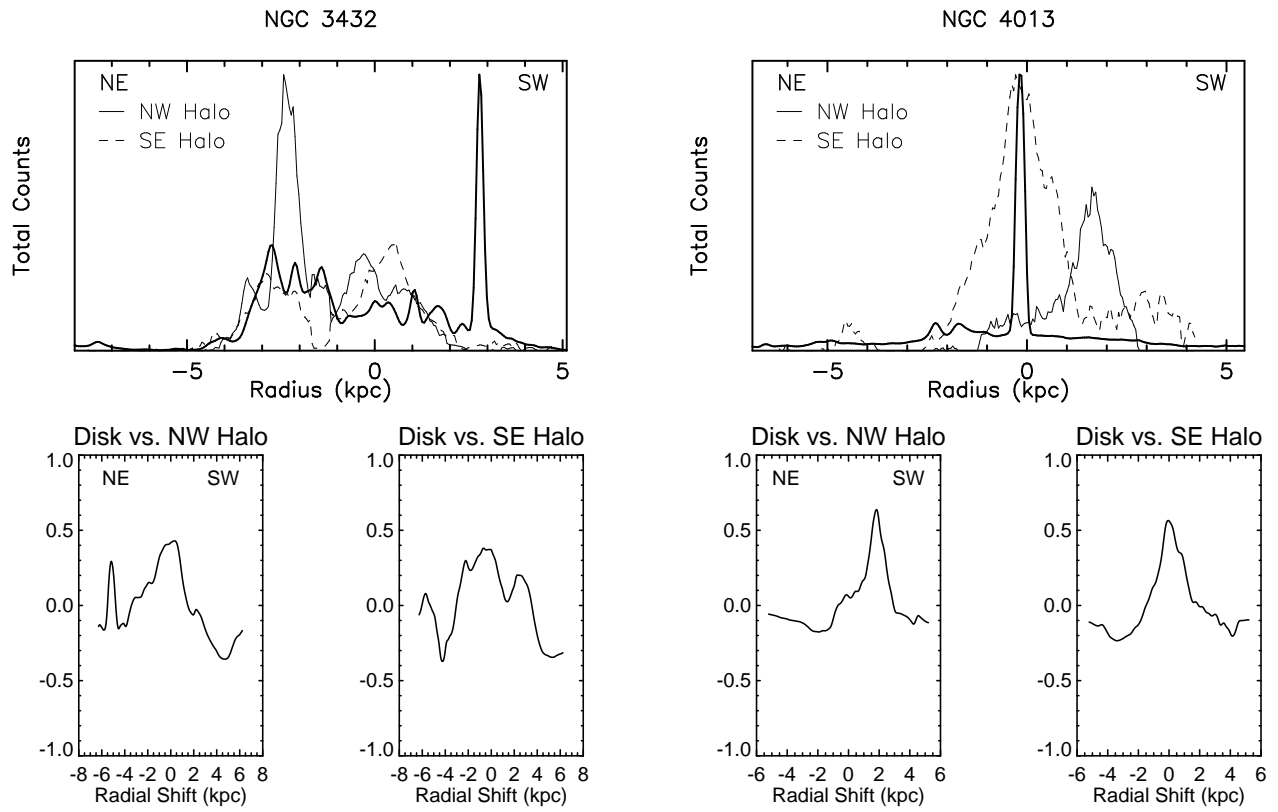


FIG. 20MN.— (Cont'd)

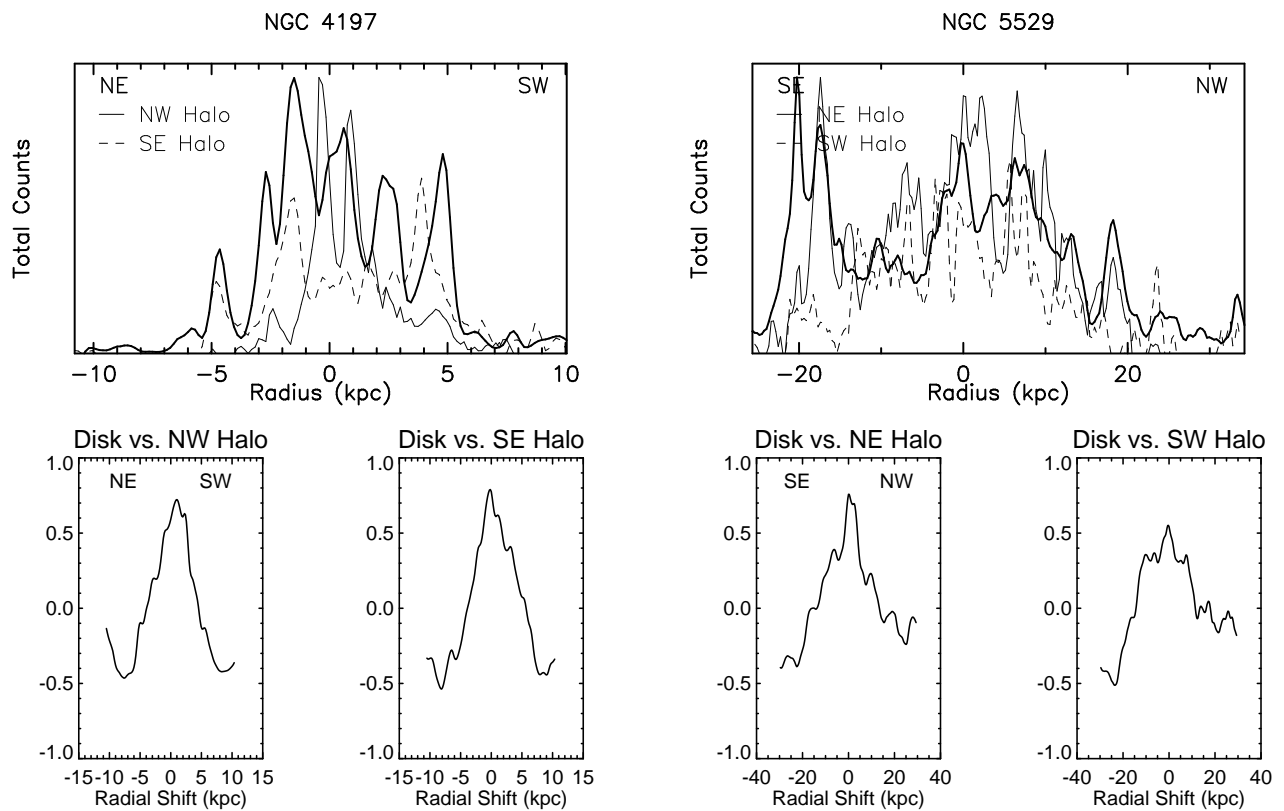


FIG. 20OP.— (Cont'd)

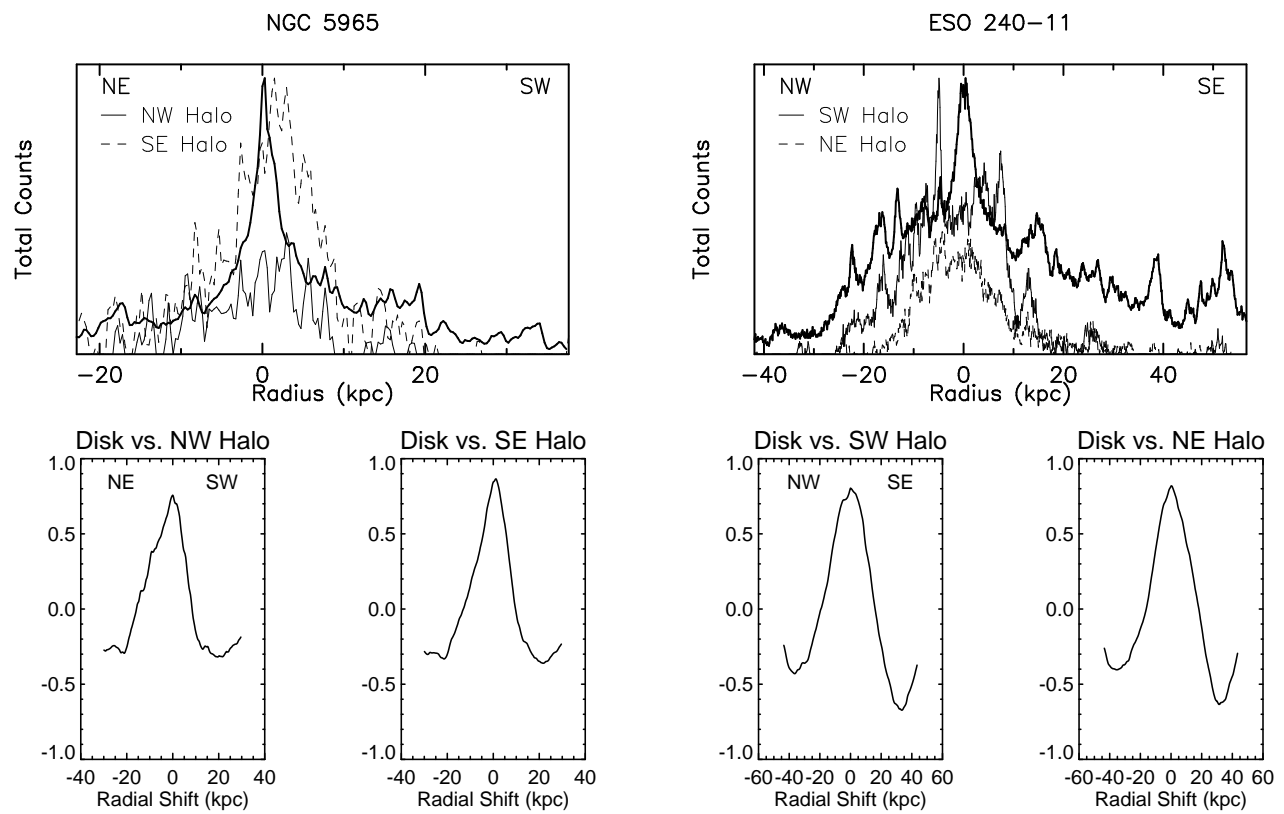


FIG. 20QR.— (Cont'd)

TABLE 1
SAMPLE.

Galaxy	R.A. (J2000) ^a hh mm ss	Dec (J2000) ^a dd mm ss	D ₂₅ ^a (arcmin)	Position ^a Angle	Galaxy ^a Type	Distance ^b (Mpc)	Incl. ^a (deg.)	L _{FIR} /D ₂₅ ^{2 c} (10 ⁴⁰ erg s ⁻¹ kpc ⁻²)	L _{IR} /D ₂₅ ^{2 c}	$\frac{L_{25}}{60}$ ^c	$\frac{L_{60}}{100}$ ^c
NGC 7817	00 03 59.0	+20 45 00	3.55	45	SABc	20.6 ^d	79	8.40	15.88	0.11	0.33
NGC 55	00 15 08.5	-39 13 13	32.36	108	SBm	1.6	90	0.04	0.09	0.14	0.22
NGC 891	02 22 33.1	+42 20 48	13.49	22	Sb	9.6	89 ^e	4.76	7.27	0.02	0.23
NGC 973	02 34 20.2	+32 30 20	3.72	48	Sbc	63 ^d	84 ^e	2.13	4.92	0.18	0.45
NGC 1507	04 04 27.3	-02 11 17	3.63	11	SB(s)m	10.6	80 ^e	2.12	4.88	0.17	0.39
ESO 362-11	05 16 39.2	-37 06 00	4.47	76	Sbc	15.4	90	2.92	5.61	0.12	0.33
NGC 2188	06 10 09.6	-34 06 22	4.37	175	SB(s)m	7.9	86	1.88	3.97	0.12	0.43
NGC 2424	07 40 39.8	+39 13 59	3.80	81	SB(r)b	44.1 ^d	82 ^e	1.11	3.30	0.36	0.29
ESO 209-9	07 58 14.9	-49 51 06	6.17	152	SB(s)cd	12.8	90	4.60	7.50	0.05	0.30
NGC 2820	09 21 47.1	+64 15 29	4.07	59	SB(s)c	20.0 ^d	90	4.09	7.30	0.07	0.34
NGC 3044	09 53 39.8	+01 34 46	4.90	13	SB(s)c	20.6	90	6.75	12.32	0.12	0.46
NGC 3432	10 52 31.3	+36 37 08	6.76	38	SB(s)m	7.8	84 ^e	1.92	3.27	0.06	0.33
NGC 4013	11 58 31.7	+43 56 48	5.25	66	Sb	17.0	90 ^e	4.60	7.46	0.05	0.24
NGC 4197	12 14 38.3	+05 48 21	3.39	36	Sc	23.1 ^d	79 ^e	3.04	6.66	0.18	0.37
NGC 5529	14 15 34.1	+36 13 36	6.17	115	Sc	43.9	90	1.17	2.74	0.15	0.24
NGC 5965	15 34 02.1	+56 41 10	5.25	53	Sb	45.6 ^d	85 ^e	0.44	1.52	0.46	0.28
ESO 240-11	23 37 49.4	-47 43 35	5.25	129	Sb	34.9	90	1.00	2.32	0.27	0.18

^aValues taken from de Vaucouleurs et al. (1991).

^bValues taken from Tully (1988) unless otherwise noted.

^cL_{IR} and L_{FIR} are calculated using the prescriptions listed in Sanders & Mirabel (1996). A value of C = 1 was used in the calculation of L_{FIR}. The IRAS fluxes used for the calculations are from Moshir et al. (1995).

^dReferences for distances: NGC 7817 (Tully, Shaya, & Pierce 1992), NGC 973 (Gourgoulhon, Chamaraux, & Fouqué 1992), NGC 2424 (Vallee 1991), NGC 2820 (Hummel & van der Hulst 1989), NGC 4197 (Guthrie 1992), NGC 5965 (Vallee 1991). The distances for NGC 973, NGC 2424, and NGC 5965 assume $H_0 = 75$ km s⁻¹ Mpc⁻¹, while the others are based on the Tully-Fisher relation.

^eReferences for inclinations: NGC 891 (Swaters 1994), NGC 973 (Guthrie 1992), NGC 1507 (Aaronson et al. 1982), NGC 2424 (Guthrie 1992), NGC 3432 (Aaronson et al. 1982), NGC 4013 (Bottema 1995), NGC 4197 (Yasuda et al. 1997), NGC 5965 (Guthrie 1992).

TABLE 2
OBSERVING LOGS FOR CONVENTIONAL NARROWBAND IMAGING.

Galaxy	Date of Observation	Telescope ^a	Filter CWL/FWHM(Å)	Exposure Time	# of Exp.	Resolution ^b ('' pixel ⁻¹)	FOV	Flux Limit (erg s ⁻¹ cm ⁻² arcsec ⁻²)
NGC 55	Dec. 1997	CTIO	6567/68	4.0 hours	20	2.03	69'0 × 69'0	11 × 10 ⁻¹⁸
NGC 973	Dec. 1997	KPNO	6653/68	4.2 hours	26	1.34	22'9 × 22'9	9 × 10 ⁻¹⁸
NGC 2424	Dec. 1997	KPNO	6618/74	3.8 hours	23	1.34	22'9 × 22'9	6 × 10 ⁻¹⁸
ESO 209-9	Dec. 1997	CTIO	6567/68	4.1 hours	17	2.03	69'0 × 69'0	18 × 10 ⁻¹⁸
NGC 2820	Dec. 1997	KPNO	6573/67	4.4 hours	27	1.34	22'9 × 22'9	5 × 10 ⁻¹⁸
NGC 3044	Dec. 1997	CTIO	6600/67	2.8 hours	15	2.03	69'0 × 69'0	13 × 10 ⁻¹⁸
NGC 3432	Dec. 1997	KPNO	6573/67	3.7 hours	22	1.34	22'9 × 22'9	8 × 10 ⁻¹⁸
NGC 4197	Apr. 1998	KPNO	6618/74	4.2 hours	24	1.34	22'9 × 22'9	7 × 10 ⁻¹⁸
NGC 5529	Apr. 1998	KPNO	6618/74	3.8 hours	23	1.34	22'9 × 22'9	8 × 10 ⁻¹⁸
NGC 5965	Apr. 1998	KPNO	6618/74	3.8 hours	23	1.34	22'9 × 22'9	10 × 10 ⁻¹⁸

^aThe KPNO telescope used for these observations was the 0.9-meter, while the 0.9-meter Curtis Schmidt telescope was used at Cerro Telolo.

^bAfter binning.

TABLE 3
OBSERVING LOGS FOR TTF IMAGING.

Galaxy	Date of Observation	Telescope	Filter CWL/FWHM(Å)	Bandpass FWHM(Å)	Exposure Time	# of Exp.	Resolution ('' pixel ⁻¹)	FOV	Flux Limit (erg s ⁻¹ cm ⁻² arcsec ⁻²)
NGC 7817	Jan. 1998	WHT	6680/280	14.9	1.0 hours	2	0.58	7'7 × 7'7	5 × 10 ⁻¹⁸
NGC 55	Dec. 1997	AAT	6680/210	13.9	1.5 hours	3	0.315	8'8 × 7'2	2 × 10 ⁻¹⁸
NGC 891	Jan. 1998	WHT	6680/280	15.7	0.8 hours	3	0.58	7'7 × 7'7	5 × 10 ⁻¹⁸
NGC 1507	Jan. 1998	WHT	6680/280	16.1	1.5 hours	3	0.58	7'7 × 7'7	5 × 10 ⁻¹⁸
ESO 362-11	Dec. 1997	AAT	6680/210	13.5	1.5 hours	3	0.594	16'5 × 13'5	4 × 10 ⁻¹⁸
NGC 2188	Dec. 1997	AAT	6680/210	13.9	1.3 hours	3	0.315	8'8 × 7'2	3 × 10 ⁻¹⁸
NGC 2424	Jan. 1998	WHT	6680/280	14.9	1.0 hours	2	0.58	7'7 × 7'7	5 × 10 ⁻¹⁸
NGC 3044	Jan. 1998	WHT	6680/280	15.7	1.0 hours	3	0.58	7'7 × 7'7	5 × 10 ⁻¹⁸
NGC 4013	Jan. 1998	WHT	6680/280	16.1	1.0 hours	2	0.58	7'7 × 7'7	7 × 10 ⁻¹⁸
ESO 240-11	Dec. 1997	AAT	6680/210	13.5	1.5 hours	3	0.594	16'5 × 13'5	5 × 10 ⁻¹⁸

TABLE 4
CALCULATED PROPERTIES OF THE GALAXIES

Galaxy	Telescope	$L_{H\alpha}(\text{total})^a$ (10^{39} erg s $^{-1}$)	$L_{H\alpha}(\text{total})/D_{25}^2$ (10^{37} erg s $^{-1}$ kpc $^{-2}$)	$L_{H\alpha}(\text{eDIG})^b$ (10^{39} erg s $^{-1}$)	$L_{H\alpha}(\text{eDIG})/L_{H\alpha}(\text{total})$ (%)
NGC 7817	WHT	22.4	5.0	2.4	11
NGC 55	CTIO	8.9	3.9	0.17	5
NGC 55 ^b	AAT	–	–	–	–
NGC 891 ^c	WHT	15.1	1.1	–	–
NGC 973 ^d	KPNO	39.6	0.8	6.3	16
NGC 1507	WHT	49.8	39.8	5.4	11
ESO 362-11	AAT	3.4	0.8	0.12	3
NGC 2188 ^b	AAT	9.9	9.8	1.3	13
NGC 2424	KPNO	30.3	1.3	4.1	13
NGC 2424	WHT	33.2	1.4	4.5	14
NGC 2820	KPNO	11.3	2.0	1.8	16
NGC 3044	CTIO	89.4	10.4	14.3	16
NGC 3044	WHT	83.2	9.6	13.3	16
NGC 3432	KPNO	20.3	8.6	1.3	6
NGC 4013	WHT	21.9	3.2	1.4	6
NGC 4197	KPNO	24.7	4.8	3.2	13
NGC 5529	KPNO	48.3	0.8	7.6	16
NGC 5965	KPNO	47.3	1.0	7.7	16
ESO 240-11	AAT	62.6	2.2	9.5	15

^aTypical error bars on the total luminosities are $\sim 10\%$ but can reach 25% due to uncertainties in the continuum subtraction. The corresponding uncertainties on the eDIG luminosities are $\sim 15\%$ and $\sim 30\%$, respectively

^bThe AAT observations of NGC 55 and NGC 2188 do not fully encompass the galaxy, so it is not possible to determine the global quantities from these observations.

^cThe presence of reflective ghosts in the image of NGC 891 prevents us from calculating some of the eDIG properties for this object.

^dThe presence of a bright star close to the NE side of NGC 973 makes sky subtraction and detection of faint emission difficult in this area. Therefore, some of the calculated galaxy properties for NGC 973 are lower limits, as determined by the unaffected portion of the galaxy.

TABLE 5
CALCULATED PROPERTIES OF GALAXIES BASED ON EXPONENTIAL FITS

Galaxy	Side	One-exponential Fit ^a				Two-exponential Fit				Total eDIG Mass ^c ($10^6 M_{\odot}$)	Recombination Rate ^d ($10^6 \text{ s}^{-1} \text{ cm}^{-2}$)
		EM ^b @ $z = 0$ (pc cm^{-6})	Scale Height (kpc)	n_e @ $z = 0$ (cm^{-3})	"Disk" Mass ^c ($10^6 M_{\odot}$)	EM ^b @ $z = 0$ (pc cm^{-6})	Scale Height (kpc)	n_e @ $z = 0$ (cm^{-3})	eDIG Mass ^c ($10^6 M_{\odot}$)		
NGC 7817	NW	520.4	0.272	0.721	57.49						
	NW	806.4	0.208	0.897	54.73	13.32	1.698	0.115	57.43		3.57
	SE	378.5	0.341	0.615	61.51						
NGC 55	SE	470.3	0.282	0.685	56.67	10.15	1.902	0.101	56.17	113.6	3.08
	NE	243.4	0.218	0.493	31.54						
	NE	1455.	0.099	1.205	35.00	52.43	0.373	0.229	25.01		3.11
NGC 891	SW	1252.	0.136	1.118	44.61						
	SW	9146.	0.080	3.022	71.00	33.03	0.451	0.182	24.00	49.01	2.37
	NW	93.71	0.864	0.306	77.28						
NGC 973	NW	43.88	0.258	0.209	15.83	69.01	1.072	0.263	82.31		11.8
	SE	85.71	1.015	0.293	87.34						
	SE	44.48	1.015	0.211	62.77	41.23	1.015	0.203	60.45	142.8	6.65
NGC 1507	NW	5.45	1.513	0.074	32.74						
	NW	4.62	1.374	0.068	27.39	0.71	5.047	0.027	39.40		0.585
	SE	5.02	1.357	0.071	28.21						
ESO 362-11	SE ^e	4.67	1.292	0.068	25.89	-	-	-	-	39.40	-
	W	57.80	0.161	0.240	11.37						
	W	16.08	0.090	0.127	3.35	36.97	0.563	0.192	31.73		3.30
NGC 2188 ^f	E	97.96	0.213	0.313	19.54						
	E	50.11	0.127	0.224	8.36	36.79	0.732	0.192	41.16	72.89	4.29
	SW	8.69	1.645	0.093	44.99						
NGC 2424 ^g	S	20.31	0.693	0.142	28.97	1.35	6.802	0.037	73.52		1.48
	N	10.35	1.608	0.102	47.94						
	N	10.85	1.115	0.104	34.05	1.96	3.267	0.044	42.41	115.9	1.01
NGC 2820	W	154.3	0.312	0.392	35.94						
	W	152.7	0.194	0.390	22.24	29.97	0.884	0.173	44.86		4.20
	E	158.5	0.331	0.398	38.64						
NGC 3044 ^h	E	161.4	0.163	0.401	19.23	44.70	0.811	0.211	50.27	95.13	5.74
	N	3.15	4.806	0.056	79.17						
	N	2.34	0.380	0.048	5.39	2.02	10.834	0.045	142.6		3.49
NGC 3044 ⁱ	S	4.55	2.037	0.067	40.28						
	S	1.86	0.338	0.043	4.27	2.31	5.431	0.048	76.66	219.3	1.99
	NW	415.3	0.362	0.644	68.49						
NGC 3432	NW ^e	529.1	0.334	0.727	71.00	-	-	-	-		-
	SE	116.3	0.485	0.341	48.51						
	SE	537.6	0.268	0.733	57.62	11.09	1.079	0.105	33.30	33.30	1.89
NGC 3044 ^j	S	1176.	0.381	1.084	121.3						
	S	1242.	0.362	1.114	118.1	6.26	4.742	0.079	110.0		4.70
	N	1101.	0.298	1.049	91.73						
NGC 3044 ^k	N	1347.	0.260	1.160	88.59	12.82	2.569	0.113	85.4	195.4	5.21
	N	1235.	0.337	1.111	110.0						
	N	1522.	0.292	1.233	105.6	16.37	2.781	0.128	104.3		7.24
NGC 3432	S	1461.	0.272	1.208	96.13						
	S	2073.	0.204	1.439	86.08	61.51	1.323	0.248	96.14	200.4	12.9
	NW	35.81	0.167	0.189	9.24						
NGC 3432	NW	24.89	0.116	0.158	5.37	7.99	1.009	0.089	26.45		1.27
	SE	38.28	0.184	0.195	10.56						
	SE	29.19	0.135	0.171	6.79	6.82	1.180	0.083	28.59	55.04	1.29

TABLE 5
CALCULATED PROPERTIES OF GALAXIES BASED ON EXPONENTIAL FITS (CONT'D)

Galaxy	Side	One-exponential Fit ^a				Two-exponential Fit				Total eDIG Mass ^c ($10^6 M_{\odot}$)	Recombination Rate ^d ($10^6 \text{ s}^{-1} \text{ cm}^{-2}$)
		EM ^b @ $z = 0$ (pc cm^{-6})	Scale Height (kpc)	n_e @ $z = 0$ (cm^{-3})	"Disk" Mass ^c ($10^6 M_{\odot}$)	EM ^b @ $z = 0$ (pc cm^{-6})	Scale Height (kpc)	n_e @ $z = 0$ (cm^{-3})	eDIG Mass ^c ($10^6 M_{\odot}$)		
NGC 4013	NW	141.7	0.579	0.376	64.09						
	NW ^e	146.3	0.558	0.382	62.58	–	–	–	–	–	–
	SE	153.4	0.657	0.391	75.40						
NGC 4197	SE	175.2	0.470	0.418	57.68	21.15	1.513	0.145	64.72	64.72	5.06
	NW	8.12	0.346	0.090	9.11						
	NW	8.78	0.164	0.094	4.51	1.28	4.947	0.036	51.90		1.02
NGC 5529	SE	7.76	0.381	0.088	9.86						
	SE	6.71	0.359	0.082	8.61	1.22	4.860	0.035	49.77	101.7	0.946
	NE	56.16	1.175	0.237	81.68						
NGC 5965	NE	58.32	0.948	0.241	67.23	4.06	4.550	0.064	84.83		2.96
	SW	39.94	1.161	0.200	67.86						
	SW	85.55	0.624	0.292	53.53	3.31	6.845	0.057	115.6	200.4	3.53
ESO 240-11	NW	19.30	1.583	0.139	64.72						
	NW	17.65	1.467	0.133	57.11	1.26	11.577	0.035	120.0		2.25
	SE	13.73	1.294	0.117	44.42						
ESO 240-11	SE	9.08	0.986	0.095	27.52	3.58	6.523	0.060	114.4	234.4	3.73
	SW	31.77	2.569	0.178	134.5						
	SW	31.85	2.473	0.178	129.4	0.39	15.536	0.020	90.48		0.988
ESO 240-11	NE	41.53	1.883	0.204	112.5						
	NE	42.04	1.741	0.205	104.9	0.86	17.863	0.029	153.3	243.8	2.39

^aThe second line for each object in the "one-exponential fit" column refers to the "two-exponential fit" thin disk.

^bThe emission measure in the midplane of the galaxy is based on the $H\alpha$ intensity at $|z| = 0$, which is derived from an extrapolation of the one- or two-exponential fit to the vertical emission profiles. Equation (1) is used for the calculations. This quantity is an emission measure determined in the midplane of the disk from the observed, edge-on orientation and is an average over all radii since it is derived from the average vertical profile of each galaxy.

^cThe ionized mass is derived using equation (4).

^dThe recombination rate in a column perpendicular to the galactic plane is calculated using equation (5).

^eA two-exponential fit is not possible in this case.

^fThe AAT observation of NGC 2188 does not fully encompass the galaxy. The values listed here only take a portion of the galaxy into account, so the total ionized mass listed here should be considered a lower limit.

^gThe quantities for NGC 2424 were derived from the WHT data. The quantities derived from the KPNO data are not reliable.

^hThese quantities were derived from the CTIO data.

ⁱThese quantities were derived from the WHT data.

TABLE 6
PEAK CORRELATION COEFFICIENT BETWEEN DISK AND EXTRAPLANAR LINE EMISSION.

Galaxy	Telescope		Side 1		Side 2		
			Peak	FWHM/2 (kpc)	Peak	FWHM/2 (kpc)	
NGC 7817	WHT	NW	0.70	3.1	SE	0.70	3.0
NGC 55	CTIO	NE	0.41	1.2	SW	0.56	1.1
NGC 55	AAT	NE	0.24	0.3	SW	0.28	0.2
NGC 891 ^a	WHT	–	–	–	–	–	–
NGC 973	KPNO	NW	0.61	8.9	SE	0.66	7.4
NGC 1507	WHT	W	0.86	1.1	E	0.27	1.6
ESO 362-11	AAT	S	0.15	1.6	N	0.12	3.0
NGC 2188	AAT	W	0.72	1.7	E	0.83	1.8
NGC 2424	KPNO	N	0.70	6.1	S	0.68	6.3
NGC 2424	WHT	N	0.28	4.4	S	0.60	3.5
NGC 2820	KPNO	NW	0.63	1.6	SE	0.93	2.0
NGC 3044	CTIO	S	0.63	4.1	N	0.90	3.1
NGC 3044	WHT	S	0.49	5.0	N	0.79	2.9
NGC 3432	KPNO	NW	0.42	1.7	SE	0.37	2.2
NGC 4013	WHT	NW	0.06	0.8	SE	0.56	1.1
NGC 4197	KPNO	NW	0.59	3.9	SE	0.84	3.5
NGC 5529	KPNO	NE	0.76	10.	SW	0.54	10.
NGC 5965	KPNO	NW	0.88	8.2	SE	0.90	8.0
ESO 240-11	AAT	SW	0.84	13.	NE	0.80	15.

^aThe presence of reflective ghosts in the image of NGC 891 prevents us from determining the radial profile of the extraplanar material in this object.

TABLE 7
DEVIATIONS FROM AVERAGE VERTICAL PROFILE

Galaxy	Telescope	Side	σ	Side	σ
NGC 7817	WHT	NW	41.4	SE	2.7
NGC 55	CTIO	NE	2.6	SW	3.9
NGC 55 ^a	–	–	–	–	–
NGC 891	WHT	NW	0.94	SE	1.4
NGC 973	KPNO	NW	3.5	SE	1.9
NGC 1507	WHT	W	9.9	E	4.2
ESO 362-11	AAT	S	0.82	N	33.9
NGC 2188	AAT	W	0.82	E	0.63
NGC 2424	KPNO	N	3.7	S	4.3
NGC 2424	WHT	N	0.41	S	0.56
NGC 2820	KPNO	NW	2.1	SE	30.9
NGC 3044	CTIO	S	4.6	N	13.2
NGC 3044	WHT	S	2.6	N	0.42
NGC 3432	KPNO	NW	1.0	SE	4.9
NGC 4013	WHT	NW	22.4	SE	4.4
NGC 4197	KPNO	NW	2.0	SE	13.3
NGC 5529	KPNO	NE	11.3	SW	1.1
NGC 5965	KPNO	NW	8.3	SE	6.4
ESO 240-11	AAT	SW	116.6	NE	4.4

^aThe AAT data of NGC 55 focus only on a small portion of the galaxy, and so it is not possible to derive these quantities from this set of observations.

TABLE 8
PEARSON'S CORRELATION COEFFICIENTS AND P[NULL] VALUES BETWEEN eDIG AND GALAXY PROPERTIES.

eDIG Properties	Quantity	Galaxy Type	L_{FIR}/D_{25}^2	L_{IR}/D_{25}^2	$\frac{I_{25}}{I_{60}}$	$\frac{I_{60}}{I_{100}}$	Distance	Inclination	$L_{H\alpha}(\text{total})/D_{25}^2$
Sample: all 17 objects									
$L_{H\alpha}(\text{total})$	r	0.20	0.36	0.38	0.14	0.36	0.31	0.097	0.313
	P[null]	0.43	0.16	0.13	0.58	0.15	0.23	0.71	0.22
$L_{H\alpha}(\text{total})/D_{25}^2$	r	0.56	0.49	0.47	0.50	0.76	0.62	0.335	—
	P[null]	0.028	0.062	0.079	0.057	0.0010	0.015	0.22	—
$L_{H\alpha}(\text{eDIG})$	r	0.25	0.34	0.36	0.19	0.36	0.36	0.174	0.184
	P[null]	0.34	0.19	0.16	0.46	0.16	0.15	0.51	0.48
$L_{H\alpha}(\text{eDIG})/H_{\alpha}L(\text{tot})$	r	0.12	0.006	0.032	0.36	0.12	0.44	0.042	0.997
	P[null]	0.66	0.98	0.90	0.15	0.65	0.080	0.87	0.71
EM ($z=0$)	r	0.14	0.54	0.53	0.28	0.37	0.30	0.195	0.501
	P[null]	0.60	0.024	0.030	0.28	0.14	0.24	0.45	0.024
Scale Height	r	0.69	0.37	0.34	0.59	0.24	0.72	0.126	0.365
	P[null]	0.0021	0.14	0.19	0.012	0.36	0.00098	0.63	0.11
n_e ($z=0$)	r	0.18	0.60	0.57	0.40	0.31	0.40	0.173	0.541
	P[null]	0.48	0.011	0.017	0.011	0.22	0.11	0.51	0.014
eDIG Ionized Mass	r	0.25	0.88	0.85	0.40	0.32	0.22	0.287	0.259
	P[null]	0.33	0.0000041	0.0000014	0.011	0.20	0.45	0.26	0.27
Sigma ^a	r	0.10	0.005	0.009	0.079	0.27	0.10	0.135	0.111
	P[null]	0.63	0.98	0.97	0.71	0.20	0.64	0.57	0.62
Sample: 10 objects (excluding NGC 55 and galaxies with $i < 85^\circ$)									
$L_{H\alpha}(\text{total})$	r	0.313	0.474	0.518	0.243	0.317	0.443	0.123	0.516
A	P[null]	0.38	0.17	0.13	0.50	0.37	0.20	0.73	0.13
$L_{H\alpha}(\text{total})/D_{25}^2$	r	0.580	0.634	0.668	0.328	0.836	0.591	0.065	—
	P[null]	0.10	0.067	0.049	0.39	0.0050	0.093	0.87	—
$L_{H\alpha}(\text{eDIG})$	r	0.255	0.432	0.483	0.281	0.345	0.448	0.091	0.503
	P[null]	0.48	0.21	0.16	0.43	0.33	0.19	0.80	0.14
$L_{H\alpha}(\text{eDIG})/H_{\alpha}L(\text{tot})$	r	0.393	0.164	0.133	0.325	0.058	0.238	0.140	0.104
	P[null]	0.26	0.65	0.71	0.36	0.87	0.51	0.70	0.78
EM ($z=0$)	r	0.147	0.434	0.370	0.507	0.232	0.625	0.092	0.564
	P[null]	0.56	0.072	0.13	0.032	0.35	0.0056	0.72	0.0050
Scale Height	r	0.172	0.568	0.537	0.672	0.550	0.632	0.009	0.488
	P[null]	0.50	0.014	0.022	0.0023	0.018	0.0049	0.97	0.055
n_e ($z=0$)	r	0.208	0.515	0.455	0.580	0.341	0.674	0.094	0.729
	P[null]	0.41	0.029	0.058	0.012	0.17	0.0022	0.71	0.0013
eDIG Ionized Mass	r	0.292	0.592	0.618	0.579	0.234	0.639	0.001	0.115
	P[null]	0.24	0.0096	0.0062	0.012	0.35	0.0043	1.00	0.67
Sigma ^a	r	0.042	0.233	0.229	0.190	0.337	0.200	0.203	0.248
	P[null]	0.86	0.32	0.33	0.42	0.15	0.40	0.39	0.32

^aSigma represents the deviation from the average profile listed in Table 7.

This figure "f1.jpg" is available in "jpg" format from:

<http://arxiv.org/ps/astro-ph/0305026v1>

This figure "f2.jpg" is available in "jpg" format from:

<http://arxiv.org/ps/astro-ph/0305026v1>

This figure "f3.jpg" is available in "jpg" format from:

<http://arxiv.org/ps/astro-ph/0305026v1>

This figure "f4.jpg" is available in "jpg" format from:

<http://arxiv.org/ps/astro-ph/0305026v1>

This figure "f5.jpg" is available in "jpg" format from:

<http://arxiv.org/ps/astro-ph/0305026v1>

This figure "f6.jpg" is available in "jpg" format from:

<http://arxiv.org/ps/astro-ph/0305026v1>

This figure "f7.jpg" is available in "jpg" format from:

<http://arxiv.org/ps/astro-ph/0305026v1>

This figure "f8.jpg" is available in "jpg" format from:

<http://arxiv.org/ps/astro-ph/0305026v1>

This figure "f9.jpg" is available in "jpg" format from:

<http://arxiv.org/ps/astro-ph/0305026v1>

This figure "f10.jpg" is available in "jpg" format from:

<http://arxiv.org/ps/astro-ph/0305026v1>

This figure "f11.jpg" is available in "jpg" format from:

<http://arxiv.org/ps/astro-ph/0305026v1>

This figure "f12.jpg" is available in "jpg" format from:

<http://arxiv.org/ps/astro-ph/0305026v1>

This figure "f13.jpg" is available in "jpg" format from:

<http://arxiv.org/ps/astro-ph/0305026v1>

This figure "f14.jpg" is available in "jpg" format from:

<http://arxiv.org/ps/astro-ph/0305026v1>

This figure "f15.jpg" is available in "jpg" format from:

<http://arxiv.org/ps/astro-ph/0305026v1>

This figure "f16.jpg" is available in "jpg" format from:

<http://arxiv.org/ps/astro-ph/0305026v1>

This figure "f17.jpg" is available in "jpg" format from:

<http://arxiv.org/ps/astro-ph/0305026v1>